

# High-order discontinuous Galerkin approximation for a three-phase incompressible Navier–Stokes/Cahn–Hilliard model

Juan Manzanero · Carlos Redondo · Miguel  
Chávez–Módena · Gonzalo Rubio · Eusebio Valero ·  
Susana Gómez–Álvarez · Ángel Rivero–Jiménez

Received: date / Accepted: date

**Abstract** In this work we introduce the development of a three-phase incompressible Navier–Stokes/Cahn–Hilliard numerical method to simulate three-phase flows, present in many industrial operations. The numerical method is then applied to successfully solve oil transport problems, such as those found in the oil and gas industry. The three-phase model adopted in this work is a Cahn–Hilliard diffuse interface model, which was derived by Boyer and Lapuerta [1]. The Cahn–Hilliard model is coupled to the entropy-stable incompressible Navier–Stokes equations model derived by Manzanero et al. [2]. The spatial discretization uses a high-order discontinuous Galerkin spectral element method which yields highly accurate results in arbitrary geometries, while an implicit–explicit (IMEX) method is adopted as temporal discretization. The developed numerical tool is tested for two and three dimensional problems, including a convergence study, a two-dimensional jet, a three-dimensional annular flow, and realistic geometries like T-shaped pipe intersections.

**Keywords** Navier–Stokes · Cahn–Hilliard · Computational fluid dynamics · High-order methods · Discontinuous Galerkin · Three-phase flows · Oil and gas transport.

## 1 Introduction

The transportation of hydrocarbons from the reservoir to the processing facilities is characterized by the modification on flowing pressure and temperature conditions. These changes in operational conditions lead to a transition from typical one-phase behavior to a more complex multiphase flow with different number of phases present along the production system (wells, flowlines, export lines,...). The vast majority of the reservoirs present fluids which evolve into a mixture of liquid crude oil, natural gas and water.

---

Juan Manzanero (E-mail: [juan.manzanero@upm.es](mailto:juan.manzanero@upm.es)), Carlos Redondo, Miguel Chávez–Módena, Gonzalo Rubio, Eusebio Valero

ETSIAE-UPM - School of Aeronautics, Universidad Politécnica de Madrid. Plaza Cardenal Cisneros 3, E-28040 Madrid, Spain. // Center for Computational Simulation, Universidad Politécnica de Madrid, Campus de Montegancedo, Boadilla del Monte, 28660, Madrid, Spain.

Susana Gómez–Álvarez, Ángel Rivero–Jiménez

Repsol Technology Lab Agustín de Betancourt S/N, 28935, Móstoles, Madrid, Spain

In case flowing bottom hole pressures at the near well location are below certain values, even sand particles or fines can be dragged and produced with the stream, leading to a more complex flow.

The physical phenomena associated with hydrocarbon multiphase flow transport (e.g., change in the flow pattern or phase change) will impact the production process or even lead to safety issues (e.g., liquid overflowing in process facilities due to an underestimation of liquid surges caused by slug flow). Therefore, an accurate prediction of the flow distribution and behaviour is mandatory to ensure reliable and continuous transport of the production fluid. In the last years, the numerical simulation of multiphase flows has become more frequent as it permits to conduct numerical experiments for many industries, such as energy, automotive or aerospace. This is due both to the improvements in multiphase flow models and the increase in computational power with HPC facilities (which, at the same time, limits its application in daily or routine engineering analysis). The petroleum industry can take advantage from high fidelity multiphase flow simulation tools to minimize the cost of production system design as well as to support the optimization of its operation.

In the oil and gas industry, multiphase flows are usually modelled with one-dimensional (1D) simulations tools (e.g. OLGA<sup>®</sup>, Pipesim<sup>®</sup> or LedaFlow<sup>®1</sup>). These models rest on a large number of experimental databases, which results in a high accuracy of the predicted results with a low computational cost [3]. However these 1D modeling tools are limited as they cannot capture some physical details, specially where three-dimensional effects are important. This means that resolving fast transient phenomena (e.g., slug flow) still presents limitations in current 1D modeling tools [4]. A different approach is followed by multiphase flow simulation based on Computational Fluid Dynamics (CFD), that permits detailed three-dimensional (3D) simulations of immiscible fluids including effects of pressure, temperature and liquid-gas heat and mass transfer. The main objectives of these simulations is to provide detailed qualitative and quantitative evaluation of flow assurance issues such as erosion or slugging, supporting designers and operators to solve flow problems or to extend the life of the flow lines.

Interface capturing methods are among the simplest approaches to treat multiphase flows in CFD. In these models, the governing equations are the continuity and momentum equations for a divergence-free velocity field, in conjunction with a convective equation that tracks the interface. Amongst interface capturing methods, such as Volume of Fluid (VOF) [5] or Level Set [6]; Diffuse Interface (DI) methods (also known as phase field methods) [7, 8, 9] provide a useful alternative that does not seem to suffer from problems with either mass conservation or the accurate computation of surface tension. Although there are examples of three phase flows (or in general, N-phase flows, with N greater or equal than 3) with Level Set or VOF methods [10, 11, 12, 13, 14, 15, 16, 17, 18], most of the work in three phase flows is based on DI methods [1, 19, 20, 21, 22, 23, 24, 25, 26, 27, 28, 29]. In this paper we focus in the phase field approach.

In DI methods, a phase-field function that describes the N-phase system is defined. The sharp fluid interface is replaced by a smooth transition layer that connects the two immiscible fluids. The free-energy, which represents the effect of the surface tension between the different fluids, is used to characterize the system. The free-energy presents two terms whose effect tend to mix the fluids and separate the fluids respectively [30, 31]. The evolution of the phase-field function in our work is modelled by means of the convective Cahn-Hilliard (CH) equation [32]. The use of the CH equation for the evolution of the

---

<sup>1</sup> OLGA<sup>®</sup>/ Pipesim<sup>®</sup> are registered trademarks of Schlumberger Inc. and LedaFlow<sup>®</sup> is a registered trademark of Kongsberg A/S.

phase-field function permits an accurate computation of the surface tension and the simulation of phase separation processes. In particular, in this work we use the model of Boyer et al. [1] to describe the three-phase system coupled to the incompressible Navier–Stokes (iNS) equations with variable density and artificial (or *pseudo*) compressibility [33]. A review of alternative iNS/CH models can be found in [34].

The three-phase model is numerically approximated in space with a high-order Discontinuous Galerkin Spectral Element Method (DGSEM) [35] that uses the Symmetric Interior Penalty (SIP) method [36, 37, 38, 39, 40]. The DGSEM has been used in the past to discretize multiphase (two phase) flows [41, 42, 43, 44, 45], and it is popular for its arbitrary order of accuracy [46, 35], low dissipative and dispersive errors [47, 48, 49, 50], the representation of arbitrary three-dimensional complex geometries through the use of unstructured meshes with curvilinear elements [51], efficient mesh adaptation techniques [52, 53, 54] and the design of provably stable schemes [55, 56, 57, 58, 59, 2, 44]. Previously, three component Cahn–Hilliard models have been discretized by means of the finite element method [20], local discontinuous Galerkin method [60] or spectral element method [61]. The DGSEM has been used in the past to discretize the two component Cahn–Hilliard equation [59] and the three component Cahn–Hilliard equation [62]. To the authors’ knowledge, this is the first implementation of the three component Cahn–Hilliard model [63] coupled with the Navier–Stokes equations in a discontinuous Galerkin framework. Even though the DGSEM provides us a framework to construct stable schemes, in this work we have not included a stability analysis and it is left for future work. Nevertheless, our results suggest a stable formulation that provides a robust solver.

Finally, for the discretization of time we consider a first order IMplicit–EXplicit (IMEX) time integrator. The linear fourth order spatial operator of the Cahn–Hilliard equation is solved implicitly while the non-linear second order spatial operator is treated explicitly. The solution of the fully-discrete system involves the solution of one linear system for each of the Cahn–Hilliard equations (two for the three phase system). As detailed in [62], the two linear systems are decoupled such that the Jacobian matrices are constant in time and identical for both Cahn–Hilliard equations. Therefore this method permits a resolution in which only one LU factorization is performed for the two equations.

The rest of this work is organized as follows: we write the governing equations in Sec. 2, and we construct its DG approximation and the IMEX time discretization in Sec. 3. Finally, we present numerical experiments for the two-phase version of the model in Sec. 4, and for the three-phase model in Sec. 5.

## 2 Governing equations

In this work, we couple the three-phase Cahn–Hilliard model of Boyer et al. [1, 62] to the incompressible Navier–Stokes with artificial compressibility [2]. We define the concentration of Phase  $j$  as the relative volume occupied by that phase. Thus, for three-phase flows we have that

$$c_1 + c_2 + c_3 = 1. \quad (1)$$

Henceforth, without loss of generality, we consider that the concentrations of Phases 1 and 2 can freely vary, and we compute the concentration of Phase 3 from (1). For Phases 1 and 2, the concentration is computed from the Cahn–Hilliard equation,

$$c_{i,t} + \vec{\nabla} \cdot (c_i \vec{u}) = \frac{M_0}{\Sigma_i} \vec{\nabla} \cdot \left( \vec{\nabla} \mu_i \right), \quad i = 1, 2, \quad (2)$$

where  $\vec{u} = (u, v, w)$  is the velocity field,  $M_0$ , is the mobility and  $\mu_i$  is the chemical potential of Phase  $i$ ,

$$\mu_i = \frac{12}{\varepsilon} \Sigma_i f_i - \frac{3}{4} \varepsilon \Sigma_i \vec{\nabla}^2 c_i, \quad i = 1, 2, 3, \quad (3)$$

with

$$f_i = \frac{\Sigma_T}{3\Sigma_i} \sum_{\substack{j=1 \\ j \neq i}}^3 \left( \frac{1}{\Sigma_j} \left[ \frac{\partial F_0^\sigma}{\partial c_i} - \frac{\partial F_0^\sigma}{\partial c_j} \right] \right), \quad \frac{3}{\Sigma_T} = \frac{1}{\Sigma_1} + \frac{1}{\Sigma_2} + \frac{1}{\Sigma_3}. \quad (4)$$

The chemical potentials are algebraically constrained [1],

$$\frac{\mu_1}{\Sigma_1} + \frac{\mu_2}{\Sigma_2} + \frac{\mu_3}{\Sigma_3} = 0, \quad (5)$$

where  $\Sigma_i$  and  $\varepsilon$  are positive constants called *spreading factors* and interface width, respectively. The *spreading factors* are computed from the interfacial tension between the two phases,

$$\Sigma_i = \sigma_{ij} + \sigma_{ik} - \sigma_{jk}, \quad (i, j, k) \text{ cyclical}. \quad (6)$$

Finally, as in [1], the *chemical free-energy*  $F_0^\sigma$  is a polynomial function on the concentrations,

$$F_0^\sigma = \sigma_{12} c_1^2 c_2^2 + \sigma_{13} c_1^2 c_3^2 + \sigma_{23} c_2^2 c_3^2 + c_1 c_2 c_3 (\Sigma_1 c_1 + \Sigma_2 c_2 + \Sigma_3 c_3). \quad (7)$$

The density (and all the thermodynamic variables) is computed from the concentration of the three phases,

$$\rho(c_1, c_2, c_3) = \rho_1 c_1 + \rho_2 c_2 + \rho_3 c_3 = \rho_1 c_1 + \rho_2 c_2 + \rho_3 (1 - c_1 - c_2), \quad (8)$$

where  $\rho_{1,2,3}$  are the densities of fluids 1, 2 and 3, respectively, assumed constant in space and time. The velocity field is given by the momentum equation,

$$(\rho \vec{u})_t + \vec{\nabla} \cdot (\rho \vec{u} \vec{u}) = -\vec{\nabla} p + \sum_{m=1}^3 \mu_m \vec{\nabla} c_m + \vec{\nabla} \cdot \left( \eta \left( \vec{\nabla} \vec{u} + \vec{\nabla} \vec{u}^T \right) \right) + \rho \vec{g}, \quad (9)$$

where  $\eta$  is the viscosity, computed from the (constant) equilibrium phases viscosities  $\eta_{1,2,3}$  in a similar fashion to the density (see (8)). The sum of the  $\mu_m \nabla c_m$  products is the phase field approximation of the capillary pressure, and  $\vec{g}$  is the gravity acceleration.

The pressure is computed with an artificial compressibility model [64, 65],

$$p_t + \rho_0 c_0^2 \vec{\nabla} \cdot \vec{u} = 0, \quad (10)$$

with  $\rho_0 = \max(\rho_1, \rho_2, \rho_3)$  and  $c_0$  the artificial compressibility sound speed.

The governing equations (2), (9) and (10) are written as a general advection–diffusion equation,

$$\mathbf{q}_t + \nabla \cdot \vec{\mathbf{f}}_e(\mathbf{q}) = \nabla \cdot \vec{\mathbf{f}}_v(\mathbf{q}, \nabla \mathbf{w}) + \mathbf{s}(\mathbf{q}, \nabla \mathbf{w}), \quad (11)$$

with the state vector  $\mathbf{q} = (c_1, c_2, \rho \vec{u}, p)$ , gradient variables  $\mathbf{w} = (\mu_1/\Sigma_1, \mu_2/\Sigma_2, \rho \vec{u}, p)$ , inviscid and viscous fluxes,

$$\mathbf{f}_e = \begin{pmatrix} c_1 u & c_1 v & c_1 w \\ c_2 u & c_2 v & c_2 w \\ \rho u^2 + p & \rho uv & \rho uw \\ \rho uv & \rho v^2 + p & \rho vw \\ \rho uw & \rho vw & \rho w^2 + p \\ \rho_0 c_0^2 u & \rho_0 c_0^2 v & \rho_0 c_0^2 w \end{pmatrix}, \quad \mathbf{f}_v = \begin{pmatrix} \frac{M_0}{\Sigma_1} \mu_{1,x} & \frac{M_0}{\Sigma_1} \mu_{1,y} & \frac{M_0}{\Sigma_1} \mu_{1,z} \\ \frac{M_0}{\Sigma_2} \mu_{2,x} & \frac{M_0}{\Sigma_2} \mu_{2,y} & \frac{M_0}{\Sigma_2} \mu_{2,z} \\ 2\eta s_{11} & 2\eta s_{12} & 2\eta s_{13} \\ 2\eta s_{21} & 2\eta s_{22} & 2\eta s_{23} \\ 2\eta s_{31} & 2\eta s_{32} & 2\eta s_{33} \\ 0 & 0 & 0 \end{pmatrix} \quad (12)$$



and source term,

$$\mathbf{s}(\mathbf{q}, \nabla \mathbf{w}) = \begin{pmatrix} 0 \\ \rho g_1 + \mu_1 c_{1,x} + \mu_2 c_{2,x} + \mu_3 c_{3,x} \\ \rho g_2 + \mu_1 c_{1,y} + \mu_2 c_{2,y} + \mu_3 c_{3,y} \\ \rho g_3 + \mu_1 c_{1,z} + \mu_2 c_{2,z} + \mu_3 c_{3,z} \\ 0 \end{pmatrix}. \quad (13)$$

In equation (12),  $\mathbf{s} = \frac{1}{2} (\nabla \bar{\mathbf{u}} + \nabla \bar{\mathbf{u}}^T)$  is the strain tensor.

## 2.1 Reduction of the model to a two-phase flow model

Constructed this way, the chemical potential satisfies an important consistency property: when one phase is not initially present (e.g. Phase 2), the chemical potential associated to that phase is zero [1],

$$\mu_2|_{c_2=0} = 0, \quad (14)$$

and the chemical potential associated to the other two phases, which satisfy  $c_1 + c_3 = 1$ , reduces to that of a two-phase model [1, 62]. We compute the chemical free-energy derivatives for  $c_2 = 0$ ,  $c_1 = c$ , and  $c_3 = 1 - c$ ,

$$\begin{aligned} \frac{\partial F_0^\sigma}{\partial c_1} &= 2\sigma_{13} c_1 c_3^2 = (\Sigma_1 + \Sigma_3) c_1 c_3^2 = (\Sigma_1 + \Sigma_3) c (1 - c)^2, \\ \frac{\partial F_0^\sigma}{\partial c_2} &= c_1 c_3 (\Sigma_1 c_1 + \Sigma_3 c_3) = c (1 - c) (\Sigma_1 c + \Sigma_3 (1 - c)), \\ \frac{\partial F_0^\sigma}{\partial c_3} &= 2\sigma_{13} c_1^2 c_3 = (\Sigma_1 + \Sigma_3) c_1^2 c_3 = (\Sigma_1 + \Sigma_3) c^2 (1 - c), \end{aligned} \quad (15)$$

which are replaced into the chemical potential (see (3)), defining  $c = c_j$  and  $c_k = 1 - c$ ,

$$\begin{aligned} \mu_1 \Big|_{\substack{c_1=c \\ c_2=0 \\ c_3=1-c}} &= \frac{12\Sigma_1}{\varepsilon} (c(1-c)^2 - c^2(1-c)) - \frac{3}{4}\Sigma_1\varepsilon\nabla^2 c, \\ &= \frac{\Sigma_1}{2\sigma_{13}} \left( \frac{12\sigma_{13}}{\varepsilon} \frac{d}{dc} (c^2(1-c^2)) - \frac{3}{2}\sigma_{13}\varepsilon\nabla^2 c \right) = \frac{\Sigma_1}{2\sigma_{13}} \mu^{2\text{ph}}. \end{aligned} \quad (16)$$

The three-phase flow model also reduces to a two-phase model if one of the concentrations is not present initially. If Phase 2 is not initially present,  $c_2(\vec{x}, 0) = 0$ , the second Cahn–Hilliard equation is

$$c_{2,t} = -\vec{\nabla} \cdot (c_2 \bar{\mathbf{u}}) + \frac{M_0}{\Sigma_2} \vec{\nabla}^2 \mu_2 = 0, \quad (17)$$

since  $\mu_2 = 0$  when  $c_2 = 0$ , as described in equation (14). Therefore,  $c_2(\vec{x}, t) = 0$  for  $t > 0$ , and Phase 2 will not show in later times. Whereas for Phase 1, its Cahn–Hilliard equation is simplified to

$$c_t + \nabla \cdot (c \bar{\mathbf{u}}) = M_0 \frac{\Sigma_1}{2\sigma_{13}} \nabla^2 \mu^{2\text{ph}}, \quad (18)$$

which corresponds to a two-phase Cahn–Hilliard model with an adjusted mobility,  $M_0 \frac{\Sigma_1}{2\sigma_{13}}$ .

Lastly, we check that the capillary pressure term of the three-phase flow also reduces to that of a two-phase flow. For three phases,

$$\begin{aligned}\vec{p}_c &= \mu_1 \vec{\nabla} c_1 + \mu_2 \vec{\nabla} c_2 + \mu_3 \vec{\nabla} c_3 = \mu_1 \vec{\nabla} c_1 + \frac{\Sigma_3}{\Sigma_1} \mu_1 \vec{\nabla} c_1 \\ &= \frac{\Sigma_1 + \Sigma_3}{\Sigma_1} \mu_1 \vec{\nabla} c_1 = \frac{2\sigma_{13}}{\Sigma_1} \mu_1 \vec{\nabla} c_1 = \mu^{2ph} \vec{\nabla} c.\end{aligned}\tag{19}$$

Therefore, we confirm that the approximation for the capillary pressure is identical in both models. In the second line, we used the property  $\Sigma_i + \Sigma_j = 2\sigma_{ij}$  of the spreading factors,  $\nabla c_3 = -\nabla c_1$ , and  $\mu_3/\Sigma_3 = -\mu_1/\Sigma_1$  (see (1) (5) and (6)).

We conclude that the three-phase model is a valid two-phase model if one of the three phases is not present initially.

### 3 Discontinuous Galerkin method and IMEX scheme

The evolution of the three-phase flow is driven by the two Cahn–Hilliard equations (see (2)), the momentum equation (9), and the artificial compressibility equation (10). The discretization of the spatial differential operators is performed using a nodal Discontinuous Galerkin Spectral Element Method (DGSEM), and the discretization of the time derivatives is performed using an IMplicit–EXplicit (IMEX) method. The latter combines a third order low-storage explicit Runge–Kutta RK3 method, and a first order backward and forward Euler method.

#### 3.1 Spatial discretization using the DGSEM

The system of equations (11) is approximated in space with a high-order discontinuous Galerkin method. The computational domain  $\Omega$  is tessellated in non-overlapping hexahedral elements  $e$ . Both the solution and the geometry are approximated by order  $N$  polynomials, and thus the elements can be curvilinear. We establish a transfinite mapping as in [51, 59] that transforms the unit cube  $E = [-1, 1]^3$  (known as the *reference element*) to an arbitrarily-shaped hexahedral element  $e$  (see Fig. 1). Thus, we work on the reference space  $(\xi, \eta, \zeta)$  where the reference element  $E$  is defined, and then its coordinates are related to the physical space with the mapping  $(x, y, z) = \vec{X}(\xi, \eta, \zeta)$ .

We define a set of tensor product Gauss–Lobatto (GL) points  $(\xi_i, \eta_j, \zeta_k)_{i,j,k=0}^N$  [35], which we use to approximate the solution by order  $N$  polynomials,

$$\mathbf{q}|_e \approx \mathbf{I}^N(\mathbf{q}) = \mathbf{Q} = \sum_{i,j,k=0}^N \mathbf{Q}_{ijk}(t) l_i(\xi_i) l_j(\eta_j) l_k(\zeta_k),\tag{20}$$

where  $\mathbf{Q}_{ijk}$  are the nodal coefficients, and  $l_i$  are the Lagrange interpolating polynomials. The GL points also define quadrature rules that approximate the integrals on the reference element,

$$\langle f, g \rangle_E \approx \langle F, G \rangle_{E,N} = \sum_{i,j,k=0}^N w_{ijk} F_{ijk} G_{ijk},\tag{21}$$

where  $w_{ijk} = w_i w_j w_k$  are the tensor product quadrature weights [35].

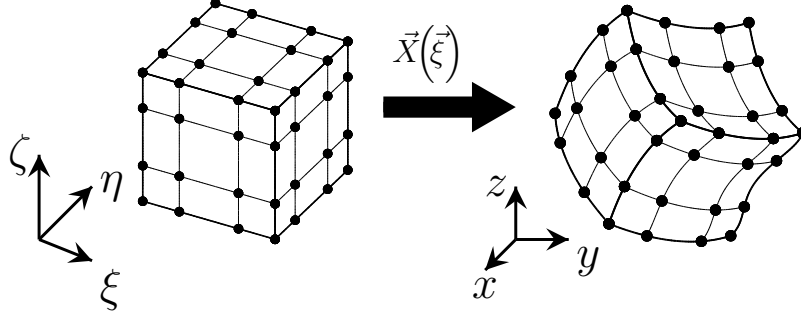


**Fig. 1** Elements geometrical transformation from the reference element  $E = [-1, 1]^3$  to their final shape and position on the physical space. The transformation uses a transfinite order  $N$  mapping  $\vec{X}(\vec{\xi})$ . The tensor product Gauss-Lobatto points are also transformed

We define the covariant and contravariant basis to relate the derivatives in the reference ( $\nabla_\xi$ ) and physical ( $\nabla$ ) spaces,

$$\vec{a}_i = \frac{\partial \vec{X}}{\partial \xi^i}, \quad \vec{a}^i = \nabla_\xi^i = \frac{\vec{a}^j \times \vec{a}^k}{J}, \quad J = \vec{a}_1 \cdot (\vec{a}_2 \times \vec{a}_3), \quad (i, j, k) \text{ cyclic}, \quad (22)$$

which allow us to compute the gradient of a scalar and the divergence of a vector as,

$$J \nabla \mathbf{w}_i = \mathcal{M} \nabla_\xi \mathbf{w}_i, \quad J \nabla \cdot \vec{\mathbf{f}}_i = \nabla_\xi \cdot \vec{\mathbf{f}}_i, \quad \vec{\mathbf{f}}_i = \mathcal{M}^T \vec{\mathbf{f}}_i, \quad \mathcal{M} = (J \vec{a}^\xi, J \vec{a}^\eta, J \vec{a}^\zeta). \quad (23)$$

Discretely, the mapping is approximated with the order  $N$  interpolation (see (20)), which is then differentiated to get the discrete covariant basis and Jacobian,  $\mathcal{J}$ . The contravariant basis, however, is computed using a curl form [51],

$$\mathcal{J} a_n^i = -\hat{x}^i \cdot \nabla_\xi \times \mathbf{I}^N (X_i \nabla_\xi X_m), \quad i, n = 1, 2, 3, \quad (n, m, l) \text{ cyclic}, \quad (24)$$

to fulfill the *discrete metric identities* [51], key to ensure the free-stream preservation (i.e. the derivative of a constant is zero) on curvilinear grids.

To construct the scheme we first cast the PDE (11) as a second order system introducing the auxiliary variable  $\vec{\mathbf{g}} = \nabla \mathbf{w}$ , and transform the operators to the reference space,

$$J \mathbf{q}_t + \nabla_\xi \cdot \vec{\mathbf{f}}_e(\mathbf{q}) = \nabla_\xi \cdot \vec{\mathbf{f}}_v(\mathbf{q}, \vec{\mathbf{g}}) + J s(\mathbf{q}, \vec{\mathbf{g}}), \quad (25)$$

$$J \vec{\mathbf{g}} = \mathcal{M} \nabla_\xi \mathbf{w}.$$

Next, we multiply equation (25) by two order  $N$  polynomial arbitrary test functions, integrate over the reference element  $E$ , and apply the Gauss law on the inviscid and viscous fluxes, and on the gradient of  $\mathbf{w}$ ,

$$\langle J \mathbf{q}_t, \phi \rangle_E + \int_{\partial e} \phi^T (\vec{\mathbf{f}}_e - \vec{\mathbf{f}}_v) \cdot d\vec{S} - \langle \vec{\mathbf{f}}_e, \nabla_\xi \phi \rangle_E = - \langle \vec{\mathbf{f}}_v, \nabla_\xi \phi \rangle_E + \langle J s, \phi \rangle_E, \quad (26)$$

$$\langle J \vec{\mathbf{g}}, \vec{\varphi} \rangle_E = \int_{\partial e} \mathbf{w}^T \vec{\varphi} \cdot d\vec{S} - \langle \mathbf{w}, \nabla_\xi \cdot \vec{\varphi} \rangle_E.$$

Now we replace the polynomial ansatz. The functions are approximated by polynomials, and the integrals by quadratures. As a result of the disconnection between adjacent elements, the solution can be discontinuous across the inter-element faces, and the fluxes at the surface integrals are not defined. Thus, we use a uniquely defined *numerical flux* at the surface integrals,  $\vec{\mathbf{f}} \approx \vec{\mathbf{f}}^*(\mathbf{q}_L, \mathbf{q}_R)$  that depend on the two neighbouring states,

$$\begin{aligned} \langle \mathcal{J}\mathbf{Q}_t, \phi \rangle_{E,N} + \int_{\partial e,N} \phi^T (\vec{\mathbf{F}}_e^* - \vec{\mathbf{F}}_v^*) \cdot d\vec{S} - \langle \vec{\mathbf{F}}_e, \nabla_\xi \phi \rangle_{E,N} &= - \langle \vec{\mathbf{F}}_v, \nabla_\xi \phi \rangle_{E,N} + \langle \mathcal{J}\mathbf{S}, \phi \rangle_{E,N}, \\ \langle \mathcal{J}\vec{\mathbf{G}}, \vec{\varphi} \rangle_{E,N} &= \int_{\partial e,N} \mathbf{W}^{*,T} \vec{\varphi} \cdot d\vec{S} - \langle \mathbf{W}, \nabla_\xi \cdot \vec{\varphi} \rangle_{E,N}. \end{aligned} \quad (27)$$

Lastly, we enhance the robustness of this implementation by using a split-form scheme [66, 55]. To do so, we apply a second time the Gauss law on the inviscid fluxes,

$$\begin{aligned} \langle \mathcal{J}\mathbf{Q}_t, \phi \rangle_{E,N} + \int_{\partial e,N} \phi^T (\vec{\mathbf{F}}_e^* - \vec{\mathbf{F}}_e - \vec{\mathbf{F}}_v^*) \cdot d\vec{S} + \langle \mathbb{D}(\vec{\mathbf{F}}_e), \phi \rangle_{E,N} &= - \langle \vec{\mathbf{F}}_v, \nabla_\xi \phi \rangle_{E,N} + \langle \mathcal{J}\mathbf{S}, \phi \rangle_{E,N}, \\ \langle \mathcal{J}\vec{\mathbf{G}}, \vec{\varphi} \rangle_{E,N} &= \int_{\partial e,N} \mathbf{W}^{*,T} \vec{\varphi} \cdot d\vec{S} - \langle \mathbf{W}, \nabla_\xi \cdot \vec{\varphi} \rangle_{E,N}, \end{aligned} \quad (28)$$

where  $\mathbb{D}(\vec{\mathbf{F}}_e)$  is a split-form approximation of the divergence  $\nabla_\xi \cdot \vec{\mathbf{F}}_e$  that uses a two-point flux  $\vec{\mathbf{F}}_e^\#$ ,

$$\mathbb{D}(\vec{\mathbf{F}}_e)_{ijk} = 2 \sum_{m=0}^N \left( D_{im} \vec{\mathbf{F}}_e(\mathbf{Q}_{ijk}, \mathbf{Q}_{mjk}) + D_{jm} \vec{\mathbf{G}}_e(\mathbf{Q}_{ijk}, \mathbf{Q}_{imk}) + D_{km} \vec{\mathbf{H}}_e(\mathbf{Q}_{ijk}, \mathbf{Q}_{ijm}) \right), \quad (29)$$

with  $D_{ij} = l'_j(\xi_i)$ . For this work, we adapt the two-point flux derived in [2] for the incompressible Navier–Stokes to the system solved herein. For the last four equations we simply copy the two-point flux from [2], and then we perform the product of the averages for the first two equations:

$$\vec{\mathbf{F}}_e^\# = \begin{pmatrix} \{c_1\} \{u\} & \{c_1\} \{v\} & \{c_1\} \{w\} \\ \{c_2\} \{u\} & \{c_2\} \{v\} & \{c_2\} \{w\} \\ \{\rho\} \{u\}^2 + \{p\} & \{\rho\} \{u\} \{v\} & \{\rho\} \{u\} \{v\} \\ \{\rho\} \{u\} \{v\} & \{\rho\} \{v\}^2 + \{p\} & \{\rho\} \{v\} \{w\} \\ \{\rho\} \{u\} \{w\} & \{\rho\} \{v\} \{w\} & \{\rho\} \{w\}^2 + \{p\} \\ \rho_0 c_0^2 \{u\} & \rho_0 c_0^2 \{v\} & \rho_0 c_0^2 \{w\} \end{pmatrix}, \quad \vec{\mathbf{F}}_{e,i}^\# = \{\mathcal{M}\} \vec{\mathbf{F}}_{e,i}^\#, \quad (30)$$

where the brackets represent the average between the two states,

$$\{\{u\}\} = \frac{u_i + u_m}{2}. \quad (31)$$

The approximation of the equations is completed with the approximation of the chemical potentials, which are the first two gradient variables  $w_1, w_2$ . To do so, we proceed as in the PDE: we cast the definition of the chemical potentials introducing auxiliary variables  $\vec{g}_{c,i} = \nabla c_i$ , we transform the differential

operators to the reference space, we construct weak forms within the elements, and integrate the volume terms with differential operators to get,

$$\begin{aligned} \langle \mathcal{J}\mu_i, \phi \rangle_{E,N} &= \left\langle \mathcal{J} \frac{12}{\varepsilon} \Sigma_i F_i, \phi \right\rangle_{E,N} - \frac{3}{4} \varepsilon \Sigma_i \int_{\partial e, N} \phi \left( \vec{G}_{c,i}^* \right) \cdot d\vec{S} + \frac{3}{4} \varepsilon \Sigma_i \left\langle \vec{G}_{c,i}, \vec{\nabla}_\xi \phi \right\rangle_{E,N}, \\ \langle \mathcal{J}\vec{G}_{c,i}, \vec{\varphi} \rangle_{E,N} &= \int_{\partial e, N} C_i^{*,T} \vec{\varphi} \cdot d\vec{S} - \left\langle C_i, \vec{\nabla}_\xi \cdot \vec{\varphi} G_c \right\rangle_{E,N}. \end{aligned} \quad (32)$$

From the concentration field  $(C_1, C_2)$ , we compute the chemical potentials  $(\mu_1, \mu_2)$ , which are then introduced in the entropy variables  $\mathbf{W}$ , to compute their gradient  $\vec{\mathbf{G}}$ , and the state vector time derivative  $\mathbf{Q}_t$ . In the next sections, we describe the computation of the numerical fluxes for inter-element and physical boundary faces.

### 3.1.1 Numerical fluxes

The numerical fluxes couple the inter-element solutions through an uniquely defined value for the surface integrals. For the inviscid Riemann solver  $\vec{\mathbf{F}}_e^*$  we compute the exact Riemann problem solution derived in [67] for the normal velocity  $u^*$  and the pressure  $p^*$ ,

$$\begin{aligned} u^* &= \frac{p_R - p_L + \rho_R u_R \lambda_R^- - \rho_L u_L \lambda_L^+}{\rho_R \lambda_R^- - \rho_L \lambda_L^+}, \quad p^* = p_R + \rho_R \lambda_R^- (u_R - u^*), \\ c_1^*, c_2^*, v^*, w^* &= \begin{cases} c_{1L}, c_{2L}, v_L, w_L & \text{if } u^* \geq 0 \\ c_{1R}, c_{2R}, v_R, w_R & \text{if } u^* < 0 \end{cases}, \end{aligned} \quad (33)$$

and we compute the tangential velocities  $v^*, w^*$  and concentrations  $c_1^*, c_2^*$  from the appropriate element depending on the sign of  $u^*$ . Amongst the beneficial properties of this Riemann solver that led to this choice, we highlight that it is physical (it is the exact solution of the Riemann problem), efficient (e.g. does not need any iterative solution) and parameter-free.

For viscous fluxes and gradient variables,  $\vec{\mathbf{F}}_v^*$  and  $\mathbf{W}^*$ , we use the Symmetric Interior Penalty (SIP) method,

$$\mathbf{W}^* = \{\{\mathbf{W}\}\}, \quad \vec{\mathbf{F}}_v^* = \left\{ \left\{ \vec{\mathbf{F}}_v \left( \mathbf{Q}, \vec{\nabla} \mathbf{W} \right) \right\} \right\} + \beta \begin{pmatrix} \frac{M_0}{\Sigma_1} \llbracket \mu_1 \rrbracket \\ \frac{M_0}{\Sigma_2} \llbracket \mu_2 \rrbracket \\ \mu \llbracket \rho \vec{u} \rrbracket \\ \mu \llbracket p \rrbracket \end{pmatrix} \vec{n}_L, \quad (34)$$

which uses the local gradient (23) for  $\vec{\nabla} \mathbf{W}$ . We take the penalty parameter from [68]

$$\beta = \frac{(N+1)(N+2)}{2\bar{h}}, \quad \bar{h} = \frac{\min(V_L, V_R)}{S}, \quad (35)$$

where  $\bar{h}$  is yields an approximated measure of the minimum element size normal to the face,  $V_L$  and  $V_R$  are the volumes of the neighbouring elements, and  $S$  is the area of the face. Finally, for the concentration and its gradient we also use the SIP method,

$$C_i^* = \{\{C_i\}\}, \quad \vec{G}_{c,i}^* = \left\{ \left\{ \vec{\nabla} C_i \right\} \right\} - \beta (C_{i,L} \vec{n}_L + C_{i,R} \vec{n}_R). \quad (36)$$

### 3.2 Time discretization

The fourth order spatial derivative in the Cahn–Hilliard equation is too stiff to be solved explicitly. Unless the mobility parameter is low enough to allow reasonable time–steps, we use an IMPLICIT–EXPLICIT (IMEX) method to integrate in time: Navier–Stokes terms are solved using a third–order explicit Runge–Kutta (RK3) method, the Cahn–Hilliard chemical free–energy is solved using forward Euler and the Cahn–Hilliard interface energy is solved using backward Euler. This first order IMEX scheme was adapted from that derived in [29] in the context of  $N$ –phase flows.

This IMEX procedure has two steps, which we describe in a semi–discrete fashion (continuous in space, discrete in time):

1. We perform the explicit RK3 step for the Navier–Stokes terms, without the contribution from the chemical–free energy and interfacial energy in the Cahn–Hilliard equation,

$$\begin{pmatrix} c_1 \\ c_2 \\ \rho \vec{u} \\ p \end{pmatrix}_t = -\nabla \cdot \begin{pmatrix} c_1 \vec{u} \\ c_2 \vec{u} \\ \rho \vec{u} \vec{u} + p \mathbf{l}_3 \\ \rho_0 c_0^2 \vec{u} \end{pmatrix} + \nabla \cdot \begin{pmatrix} 0 \\ 0 \\ \eta (\nabla \vec{u} + \nabla \vec{u}^T) \\ 0 \end{pmatrix} + \begin{pmatrix} 0 \\ 0 \\ \rho \vec{g} + \sum_{m=1}^3 \mu_m \nabla c_m \\ 0 \end{pmatrix}. \quad (37)$$

After the RK3 time–step, the variables are called  $(\hat{c}_1, \hat{c}_2, \rho \vec{u}^{n+1}, p^{n+1})$ , since the concentrations need a correction step to include the chemical potential.

2. We compute a correction step on the two concentrations to solve the Cahn–Hilliard equations. The chemical free–energy terms are solved explicitly (i.e. evaluated in  $c_i^n$ ) and the stiff interfacial energy terms implicitly (i.e. evaluated in  $c_i^{n+1}$ ). Besides, we also introduce the stabilizing term  $S_0 (c_i^{n+1} - c_i^n)$ , being  $S_0$  a constant. Finally, the approximation of the time derivative is  $c_t \approx (c_i^{n+1} - \hat{c}_i) / \Delta t$ . As a result, the IMEX correction step for each concentration is:

$$\frac{c_i^{n+1} - \hat{c}_i}{\Delta t} = M_0 \vec{\nabla}^2 \left( \frac{12}{\varepsilon} f_i(c_1^n, c_2^n, c_3^n) + S_0 (c_i^{n+1} - c_i^n) - \frac{3}{4} \varepsilon \vec{\nabla}^2 c_i^{n+1} \right). \quad (38)$$

Two decoupled linear systems for the two concentration parameters are solved. However, the linearity of the operator produces a constant in time Jacobian, which also are identical for both phases. This properties led us to compute the solution to the linear problem with LU factorization (performed only once at the preprocessing) and Gauss substitution. The latter, after the preprocessing, gets similar computational times to an iteration in a explicit method.

### 3.3 Boundary conditions

In this section we describe the imposition of inflow, outflow, and no–slip wall boundary conditions. In this work, we prescribe the boundary conditions weakly. Hence, we create a ghost (exterior) state with the appropriate boundary information, and then compute the interface fluxes between the interior  $\mathbf{Q}^i$  and exterior  $\mathbf{Q}^e$  states.

### 3.3.1 Inflow boundary condition

For the inflow boundary condition, we specify the inflow concentration  $c_{i,\text{inflow}}(\vec{x}; t)$  and the velocity  $\vec{u}_{\text{inflow}}(\vec{x}; t)$ . For the inviscid fluxes, we construct a ghost state,

$$\mathbf{Q}^e = \begin{pmatrix} C_{1,\text{inflow}} \\ C_{2,\text{inflow}} \\ \rho(C_{\text{inflow}})\vec{U}_{\text{inflow}} \\ P \end{pmatrix}, \quad (39)$$

where we take the pressure  $P$  from the interior, and compute the interface flux from the exact Riemann problem solution (see (33)),  $\vec{\mathbf{F}}_e^*(\mathbf{Q}_e^i, \mathbf{Q}_e^e)$ .

We defined the viscous fluxes as:

$$\mathbf{W}^* = \frac{\mathbf{W}^i + \mathbf{W}^e}{2}, \quad \mathbf{F}_v^* \cdot \vec{n} = \begin{pmatrix} 0 \\ 0 \\ \eta(\nabla\vec{U} + \nabla\vec{U}^T) \cdot \vec{n} \\ 0 \end{pmatrix}, \quad (40)$$

where we apply the Neumann boundary conditions to the chemical potential, and take the interior values for viscous stresses. In (40), we compute the gradient variables from the ghost state,  $\mathbf{W}^e = \mathbf{W}(\mathbf{Q}^e)$ .

The implementation features an automatic method for the distribution of the phases in a circular section, given the superficial velocities and the slip velocities. The superficial velocity of each phase is, for a given flow rate, the equivalent velocity obtained if the phase occupies the entire section,

$$v_{s,i} = \frac{1}{A_{\text{inflow}}} \int_{\text{inflow}} \vec{u}_i \cdot d\vec{S}. \quad (41)$$

Furthermore, because real flow configurations feature a large ratio of the superficial velocities that confine one of the phases to the near wall region, we allow the velocity to be discontinuous at the interface between the phases. By doing so, we can use lower velocities for the phases with smaller superficial velocity, so that they occupy a larger region of the cross section. The problem with a phase being very confined to the near wall region is that it might not be well captured by the numerical method. For the flow configuration given in Fig. 2, the concentration inflow boundary condition is

$$\begin{aligned} c_{1,\text{inflow}}(x, y) &= \frac{1}{2} + \frac{1}{2} \tanh\left(\frac{y - y_{12}}{\varepsilon}\right), \\ c_{2,\text{inflow}}(x, y) &= \frac{1}{2} \tanh\left(\frac{y - y_{23}}{\varepsilon}\right) - \frac{1}{2} \tanh\left(\frac{y - y_{12}}{\varepsilon}\right), \end{aligned} \quad (42)$$

and the velocities are computed from a Poiseuille flow,

$$u_{\text{inflow}} = (V_{1,\text{max}}c_{1,\text{inflow}} + V_{2,\text{max}}c_{2,\text{inflow}} + V_{3,\text{max}}c_{3,\text{inflow}}) \left(1 - \left(\frac{r}{R}\right)^2\right), \quad (43)$$

with the two slip velocities, which are user-input,

$$V_{s,12} = V_{1,\text{max}} - V_{2,\text{max}}, \quad V_{s,23} = V_{2,\text{max}} - V_{3,\text{max}}. \quad (44)$$

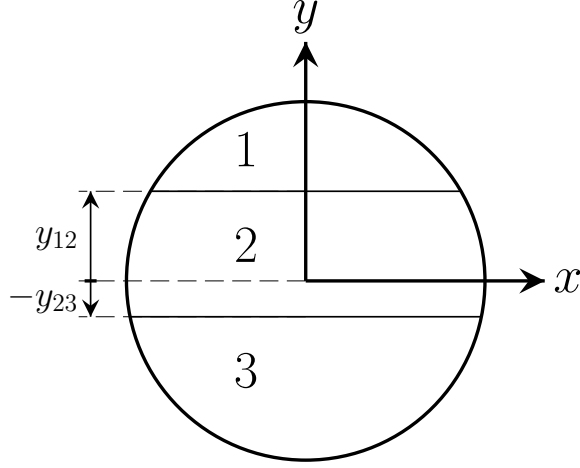


**Fig. 2** Configuration of a layered inflow. The position of the two interfaces is provided by the values  $y_{12}$  and  $y_{23}$

Therefore, there are five unknowns ( $V_{1,\max}$ ,  $V_{2,\max}$ ,  $V_{3,\max}$ ,  $y_{12}$ , and  $y_{23}$ ), and five equations: the two slip-velocities definitions (see (44)), and the superficial velocities,

$$v_{s,i} = \frac{V_{i,\max}}{A_{\text{inflow}}} \int_{\text{inflow}} c_{i,\text{inflow}} \left(1 - \left(\frac{r}{R}\right)^2\right) dS, \quad (45)$$

that are solved using a Newton–Rhapson method.

### 3.3.2 Outflow boundary condition

The outflow boundary condition specifies the ambient pressure at the exit of the domain  $P_o$ , and applies a Neumann boundary condition to the rest of the variables. Therefore, for the inviscid fluxes the exterior state is defined as:

$$\mathbf{Q}^e = \begin{pmatrix} C_1 \\ C_2 \\ \rho \vec{U} \\ P_o \end{pmatrix}, \quad (46)$$

whereas for viscous fluxes we simply use a Neumann boundary condition for all the variables,

$$\mathbf{W}^* = \mathbf{W}_i, \quad \mathbf{F}_v^* \cdot \vec{n} = 0. \quad (47)$$

### 3.3.3 No-slip wall boundary condition

We construct a ghost state with the same variables as the inside, but changing the sign of the normal velocity,

$$\mathbf{Q}^e = \begin{pmatrix} c_1 \\ c_2 \\ \rho \left( \vec{U} - 2 \left( \vec{U} \cdot \vec{n} \right) \vec{n} \right) \\ p \end{pmatrix}. \quad (48)$$



For the viscous numerical fluxes, we apply Neumann boundary conditions in all variables except velocities, which take the interior values,

$$\mathbf{W}^* = \frac{\mathbf{W}^i + \mathbf{W}^e}{2}, \quad \vec{\mathbf{F}}_v^* \cdot \vec{\mathbf{n}} = \begin{pmatrix} 0 \\ 0 \\ \eta (\nabla \vec{U} + \nabla \vec{U}^T) \cdot \vec{\mathbf{n}} \\ 0 \end{pmatrix}. \quad (49)$$

Finally, for the gradient of the concentrations  $\vec{G}_{c,i}^*$  the Neumann boundary condition is non-homogeneous if one wants to solve for arbitrary wall contact angles. Thus, we follow [69, 62] and use the following expression:

$$C_i^* = C_i, \quad \vec{G}_{c,i}^* \cdot \vec{\mathbf{n}} = F_{w,i}, \quad (50)$$

where the boundary coefficients  $F_{w,i}$  are

$$\begin{aligned} F_{w,1} &= -\frac{4}{\varepsilon} (\cos \theta_{12}^w C_1 C_2 (C_1 + C_2) + \cos \theta_{13}^w C_1 C_3 (C_1 + C_3)), \\ F_{w,2} &= -\frac{4}{\varepsilon} (-\cos \theta_{12}^w C_1 C_2 (C_1 + C_2) + \cos \theta_{23}^w C_2 C_3 (C_1 + C_3)), \end{aligned} \quad (51)$$

being the three wall contact angles  $\theta_{ij}^w$  related by the wall equilibrium constraint [69, 62],  $\sigma_{12} \cos \theta_{12}^w + \sigma_{23} \cos \theta_{23}^w = \sigma_{13} \cos \theta_{13}^w$ . For 90° angles, the coefficients  $F_{w,i}$  are zero, and the boundary condition reduces to homogeneous Neumann.

## 4 Two-phase simulations

We perform the validation of the solver in the particular case of solving a two-phase flow (i.e. as described in Sec. 2.1). We first solve a manufactured solution in Sec. 4.1, and then we solve a two-phase horizontal pipe in Sec. 4.2. The enhancement of the robustness provided by the split-form scheme is addressed in Sec. 4.3.

### 4.1 Manufactured solution

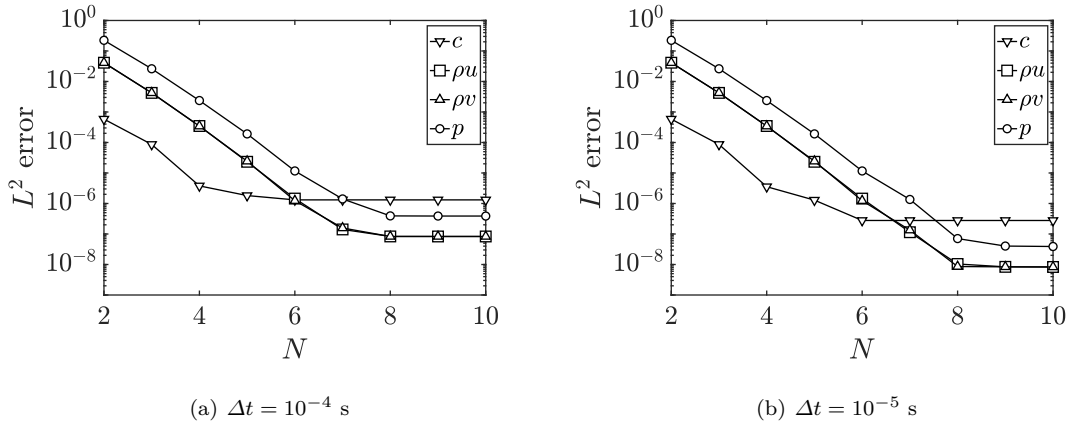
We first study the convergence properties of the method. To do this, we borrow the manufactured solution from a previous two-phase work [44]. This two-phase manufactured solution is defined as:

$$\begin{aligned} c_{1,0}(x, y; t) &= \frac{1}{2} (1 + \cos(\pi x) \cos(\pi y) \sin(t)), \\ c_{2,0}(x, y; t) &= 0, \\ u_0(x, y; t) &= 2 \sin(\pi x) \cos(\pi z) \sin(t), \\ v_0(x, y; t) &= -2 \cos(\pi x) \sin(\pi y) \sin(t), \\ p_0(x, y; t) &= 2 \sin(\pi x) \sin(\pi z) \cos(t), \end{aligned} \quad (52)$$

which we solve on the domain  $(x, y) \in [-1, 1]^2$  m. The final time is  $t_F = 0.1$  s, and all the physical parameters are presented in Table 1.

**Table 1** List of the parameter values used with the manufactured solution (see (52))

$\rho_1$	$\rho_3$ (kg/m <sup>3</sup> )	$\eta_1$	$\eta_2$ (Pa·s)	$\varepsilon$ (m)	$M_0$ (m/s)	$c_0^2$ (m/s <sup>2</sup> ) <sup>2</sup>	$\sigma$ (N/m)
1.0	2.0	1.0E-3	1.0E-3	1/√2	1.134E-2	1.0E3	6.236E-3

**Fig. 3** Two-phase solver: polynomial order convergence study of the manufactured solution (52). We represent the  $L^2$  errors in concentration,  $x$ - and  $y$ -momentum, and pressure. The polynomial order ranges from 2 to 10, and we integrate in time until  $t_F = 0.1$  s with two time step sizes:  $\Delta t = 10^{-4}$  s and  $10^{-5}$  s. All physical parameters are given in Table 1

We first present the polynomial order convergence analysis in Fig. 3 for two values of the  $\Delta t$  parameter,  $\Delta t = 10^{-4}$  s and  $10^{-5}$  s. We consider a mesh with  $4^2$  elements, and the polynomial order ranges from  $N = 2$  to  $N = 10$ . We represent the  $L^2$  errors for the concentration, momentum, and pressure. For both time-step values, the errors behave similarly, with a space under-resolved region for lower polynomial orders, where the errors decrease exponentially, and a time under-resolved region where the error stagnates with the polynomial order. We see that the use of a first order Euler scheme for the Cahn–Hilliard part impacts its accuracy, as the stagnation is reached in low polynomial orders (i.e. where temporal errors dominate). However, we believe that for an industrial solver, to achieve exponential convergence in the Cahn–Hilliard equation is not critical. The role of the Cahn–Hilliard equation for an industrial simulation is to advect the phases, to introduce interface regularization that helps to solve under-resolved simulations, and to separate the phases (or avoid the mixing). We support this argument by adding that the mobility is adjusted in practice by trial and error.

The flow variables are solved with the third order RK3 method, which leads to more accurate solutions for the momentum and pressure equations. Overall, we find a satisfactory convergence behavior of the method for smooth solutions.

We also perform a mesh convergence study, presented in Table 2. We use meshes with  $4^2$ ,  $6^2$ ,  $8^2$ ,  $12^2$ , and  $16^2$  elements, and we vary the polynomial order from  $N = 2$  to  $N = 5$ . For lower polynomial orders, we find the expected order of convergence for the Cahn–Hilliard equation (i.e. even more than  $N + 1$ ), but then the early stagnation is found as a result of the first-order Euler scheme. For the Navier–Stokes part we find that the order of accuracy is systematically between  $N$  and  $N + 1$ , which is a similar error behavior to that seen previous works [67].

**Table 2** Two-phase solver: manufactured solution (52) convergence analysis: we use five meshes with  $4^2$ ,  $6^2$ ,  $8^2$ ,  $12^2$  and  $16^2$  meshes, and  $N = 2, 3, 4$  and  $5$ . The final time is  $t_F = 0.1$  s, and we use the IMEX scheme with  $\Delta t = 5 \cdot 10^{-5}$  s

	Mesh	$c$ error	order	$\rho u$ error	order	$\rho v$ error	order	$p$ error	order
N=2	$4^2$	5.85E-04	–	4.13E-02	–	4.12E-02	–	2.24E-01	–
	$6^2$	2.61E-04	1.99	1.50E-02	2.49	1.50E-02	2.49	9.09E-02	2.22
	$8^2$	9.83E-05	3.39	7.17E-03	2.58	7.17E-03	2.58	4.71E-02	2.29
	$12^2$	2.45E-05	3.43	2.43E-03	2.67	2.43E-03	2.67	1.79E-02	2.39
	$16^2$	9.93E-06	3.13	1.10E-03	2.76	1.10E-03	2.76	8.71E-03	2.50
N=3	$4^2$	8.62E-05	–	4.23E-03	–	4.24E-03	–	2.61E-02	–
	$6^2$	1.43E-05	4.44	9.90E-04	3.58	9.90E-04	3.59	7.04E-03	3.23
	$8^2$	3.52E-06	4.87	3.40E-04	3.72	3.40E-04	3.72	2.69E-03	3.34
	$12^2$	1.41E-06	2.26	7.11E-05	3.86	7.12E-05	3.86	6.55E-04	3.48
	$16^2$	1.39E-06	0.05	2.27E-05	3.97	2.27E-05	3.97	2.31E-04	3.62
N=4	$4^2$	3.81E-06	–	3.47E-04	–	3.43E-04	–	2.37E-03	–
	$6^2$	1.66E-06	2.05	5.26E-05	4.65	5.26E-05	4.62	4.06E-04	4.36
	$8^2$	1.39E-06	0.60	1.35E-05	4.74	1.35E-05	4.73	1.12E-04	4.48
	$12^2$	1.39E-06	0.01	1.90E-06	4.83	1.91E-06	4.83	1.74E-05	4.59
	$16^2$	1.39E-06	0.00	4.63E-07	4.91	4.65E-07	4.91	4.52E-06	4.68
N=5	$4^2$	1.87E-06	–	2.33E-05	–	2.43E-05	–	1.91E-04	–
	$6^2$	1.39E-06	0.74	2.36E-06	5.64	2.37E-06	5.75	2.07E-05	5.48
	$8^2$	1.39E-06	0.00	4.60E-07	5.69	4.62E-07	5.68	4.21E-06	5.54
	$12^2$	1.39E-06	0.00	6.28E-08	4.91	6.29E-08	4.92	4.61E-07	5.45
	$16^2$	1.39E-06	0.00	4.26E-08	1.34	4.26E-08	1.35	2.10E-07	2.74

We conclude that the convergence study confirms that the error behavior of the scheme is the expected one for smooth solutions.

## 4.2 Pipe simulations

In this section, we focus on more practical test cases, relevant for the oil and gas industry. In particular, we simulate the flow in horizontal pipes with different superficial velocities (see (45)) at the inflow,  $U_L^S$  and  $U_L^L$ , which correspond to the gas and liquid respectively. Depending on the superficial velocities values, we obtain different flow regimes. This test case follows the one proposed in [70, 43] and agrees with the experimental results of [71].

The flow pattern map of Taitel & Dukler (see Fig. 4) classifies the flow regimes as stratified flow, slug flow, dispersed bubble flow and annular flow. In a stratified flow the phases are completely separated with gas in the upper part and liquid in the lower part of the pipe. In a slug flow, the waves in the flow reach the top of the pipe, eventually closing the gas path in the top. In a dispersed bubble flow, small bubbles are present in the flow, and are dispersed everywhere in the cross section. In an annular flow the liquid forms a coat all around the pipe walls. Following [70], we define four test cases that reproduce the four flow regimes, denoted with red crosses in Fig. 4, and whose superficial velocities are given in Table 3. The domain for the simulations consists of a pipe with length  $L = 1$  m and diameter  $D = 0.1$  m. The physical domain is discretized using a mesh of 8220 hexahedral elements and the solution

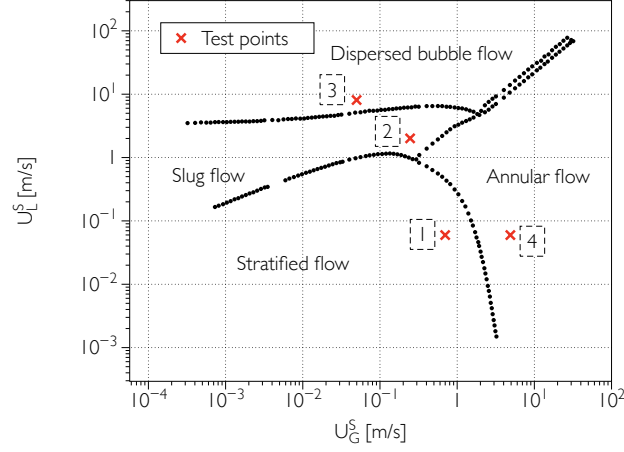


**Fig. 4** Two-phase solver: flow pattern map of the two-phase flow in a horizontal pipe with a diameter of 1 meter. The data has been extracted from [70]

**Table 3** Two-phase solver: superficial velocities (in m/s) and theoretical flow regime in horizontal pipe test case

Test	Flow regime	$U_G^S$	$U_L^S$
1	Stratified flow	0.7	0.06
2	Slug flow	0.25	2
3	Dispersed bubble flow	0.05	8
4	Annular flow	4.9	0.06

is approximated by order  $N = 3$  polynomials. The physical parameters are summarized in Table 4. The

**Table 4** Two-phase solver: physical parameters of the pipe flow

$\rho_1$	$\rho_2$ (kg/m <sup>3</sup> )	$\eta_1$	$\eta_2$ (Pa·s)	$\varepsilon$ (m)	$M_0$ (m/s)	$c_0^2$ (m/s <sup>2</sup> ) <sup>2</sup>	$\sigma$ (N/m)	$g$ (m/s <sup>2</sup> )
1.0	5.0	$5 \cdot 10^{-3}$	$10^{-2}$	0.0424	0.1886	1.0E3	$2.5 \cdot 10^{-4}$	1.0

mobility is taken from [70], and the interface width covers approximately three high-order mesh points. The time step chosen for the simulations is  $\Delta t = 10^{-5}$  s. Regarding the boundary conditions, a no-slip boundary condition (see (48)) is enforced at the pipe walls (with a contact angle of  $90^\circ$ ) while a velocity inflow boundary condition (see (39)) and a constant pressure outflow boundary condition (see (46)) are used. It should be noticed that the flow regime inflow is considered layered (see Fig. 2). The initial condition for all the simulations is propagated along the  $Z$  axis, with a small wave-like perturbation with  $Z$  coordinate, to introduce asymmetry.

Fig. 5 shows an isosurface of  $c$  values under 0.5 colored by density for the four test cases shown in Fig. 4 (organized from 1 to 4 top to bottom) at  $t = 4$  s.

In Fig. 6 we show the density contour in a  $Z$ -normal slice at  $L/D = 8$ . As can be seen, the flow regimes are correctly predicted. Note that ignoring the effect of the hydrostatic pressure at the outflow

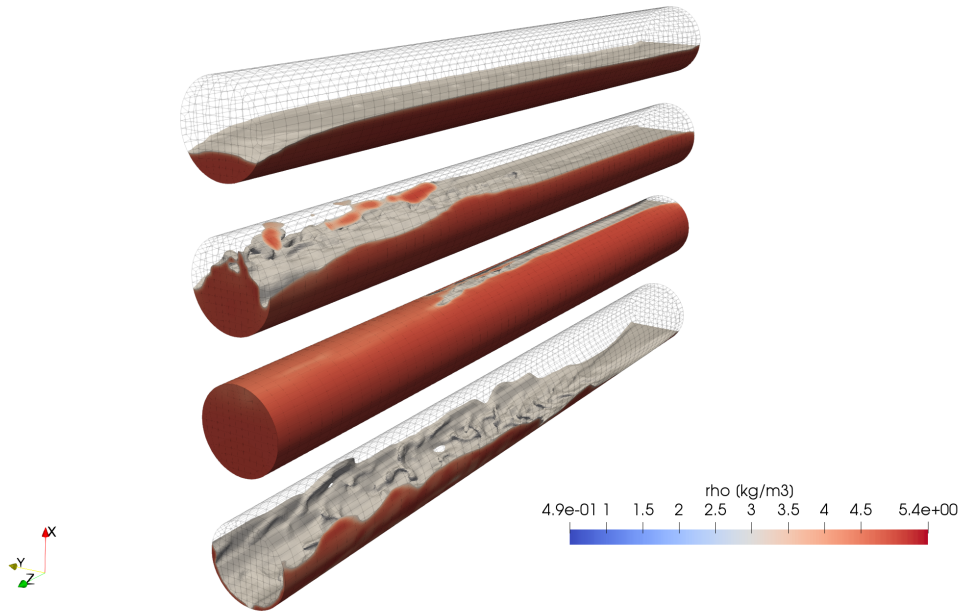


**Fig. 5** Two-phase solver: results of test cases 1-4 (organized top to bottom) at  $t = 4s$ . Stratified, Slug, Dispersed Bubble and Annular Flow regimes

when imposing a constant outlet pressure induces a velocity in the negative  $X$  direction that curves the interface. This can be more easily seen in the stratified flow regime (Test 1).

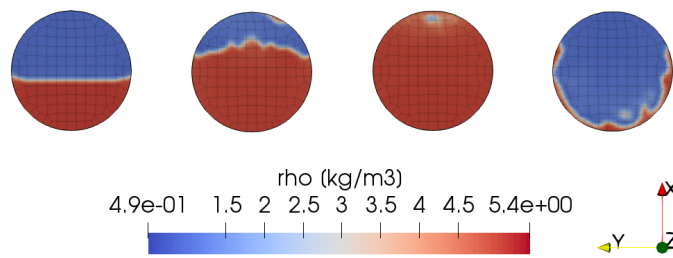


**Fig. 6** Two-phase solver: representation of the density contour in a pipe at  $z/D = 8$  cross section. The four regimes (stratified, slug, dispersed bubble, and annular) are represented.

### 4.3 Enhanced robustness of the discretization

The simulations of the flow regime prediction in pipes are under-resolved with the mesh used (except the stratified flow). Thus, this numerical experiment can be used to compare the robustness of the discretization developed in this work with the standard DG method (i.e. without the use of split-forms) with the more traditional Gauss points. Although none of the two discretizations are entropy-stable (see [72]), we see that the use of the split-form introduced herein also enhances the robustness of the multiphase solver.

We solve the four regimes with the two schemes (split-form/Gauss-Lobatto and standard/Gauss). In Fig. 7 we represent the maximum residual of the concentration ( $\max_e C_t$ ) with the number of iterations as

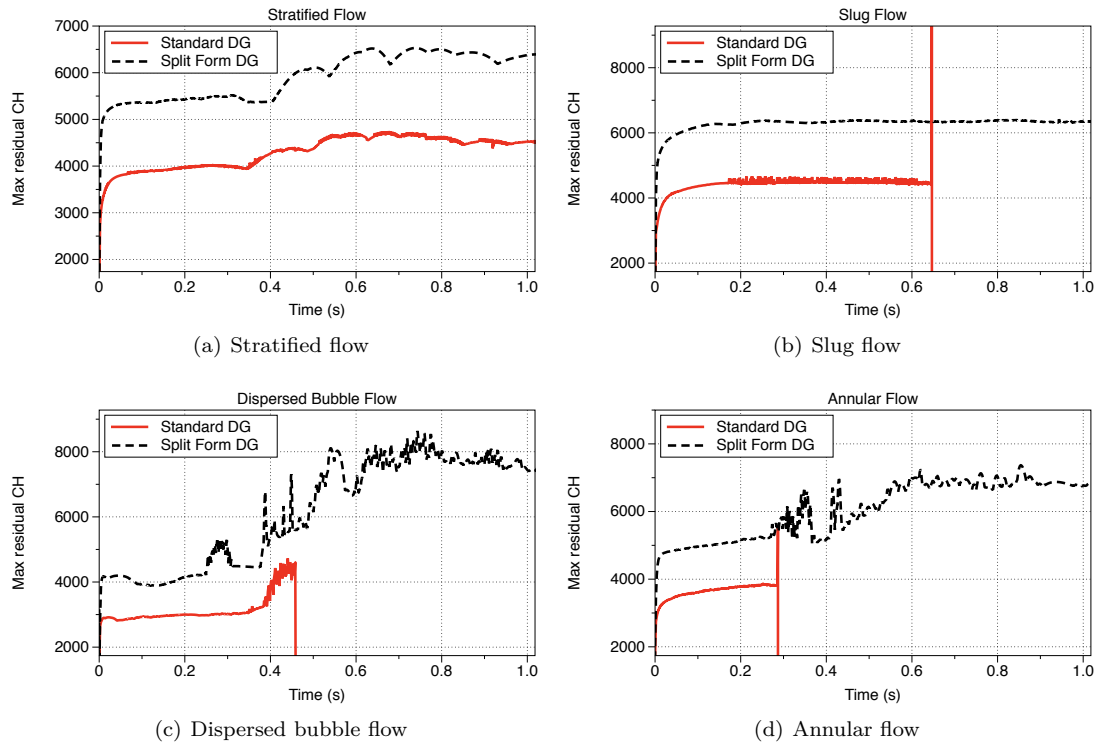


**Fig. 7** Two-phase solver: maximum value of the concentration  $c_1$  residual ( $c_{1,t}$ ) with time, for the four pipe flow regimes studied. We compare the standard DG scheme with Gauss points (solid, red line) to split-form DG (dashed, black)

a representative value of the simulation progress (as a point of reference, the steady-state is  $\max_e C_t = 0$ ). Although both methods are stable at the early stages, once the growth of fluid instabilities obtains smaller structures, the standard DG scheme with Gauss points crashes, while the split-form developed in this work is stable and allows us to obtain a final solution. Both approaches are stable for the smoother stratified flow.

We conclude that although there is no stability proof, this numerical experiment encourages the use of the split-form scheme.

## 5 Three-phase simulations

In this section we validate and test the three-phase solver. We solve a manufactured solution in Sec. 5.1, a two-dimensional horizontal channel in Sec. 5.2 and a T-shaped pipe intersection in Sec. 5.4.

### 5.1 Manufactured solution

First, we perform a manufactured solution analysis to assess the accuracy of the three-phase solver for smooth problems. We extend the two-dimensional manufactured solution used for the two-phase flow in Sec. 4.1 with the manufactured solution of the three-phase Cahn–Hilliard solver introduced in [62].

The manufactured solution now is defined as:

$$\begin{aligned}
 c_{1,0}(x, y, t) &= \frac{1}{3} (1 + \cos(\pi x) \sin(\pi y) \sin(t)), \\
 c_{2,0}(x, y, t) &= \frac{1}{3} (1 + \cos(\pi x) \sin(\pi y) \sin(1.2t)), \\
 u_0(x, y, t) &= 2 \sin(\pi x) \cos(\pi z) \sin(t), \\
 v_0(x, y, t) &= -2 \cos(\pi x) \sin(\pi y) \sin(t), \\
 p_0(x, y, t) &= 2 \sin(\pi x) \sin(\pi z) \cos(t),
 \end{aligned} \tag{53}$$

which requires an appropriate source term to the right-hand side of the equation, not presented here for simplicity. The configuration is similar to the two-phase manufactured solution, where the domain is  $(x, y) \in [-1, 1]^2$  m, and the final time is  $t_F = 0.1$  s. The physical parameters have been adapted from [29] and they are given in Table 5.

**Table 5** Three-phase solver: list of the parameter values used with the manufactured solution (see (53))

$\rho_1$	$\rho_2$	$\rho_3$ (kg/m <sup>3</sup> )	$\eta_1$	$\eta_2$	$\eta_3$ (Pa·s)	$\varepsilon$ (m)
1.0	3.0	2.0	1.0E-3	1.0E-3	1.0E-3	$1/\sqrt{2}$
<hr/>						
$M_0$ (m/s)	$c_0$ (m/s <sup>2</sup> )	$\sigma_{12}$	$\sigma_{13}$	$\sigma_{23}$ (N/m)		
1.134E-2	1.0E3	6.236E-3	7.265E-3	8.165E-3		

We perform first a polynomial order convergence study with a Cartesian mesh of  $4^2$  elements, and with the polynomial order ranging from  $N = 2$  to 10. In Fig. 8 we represent the  $L^2$  errors on the five variables ( $c_1$ ,  $c_2$ ,  $\rho u$ ,  $\rho v$  and  $p$ ), for two time-step sizes,  $\Delta t = 10^{-4}$  s and  $10^{-5}$  s. We find that the error behavior is similar to the two-phase solver, where exponential accuracy is obtained for lower polynomial orders, as expected, and then the error stagnation associated to the time discretization is anticipated for the two concentrations, as a result of the first order IMEX scheme.

Finally, we perform the mesh convergence study, where we use meshes with  $4^2$ ,  $6^2$ ,  $8^2$ ,  $12^2$  and  $16^2$  elements, and vary the polynomial order from  $N = 2$  to  $N = 5$ . The  $L^2$  errors and the convergence rates

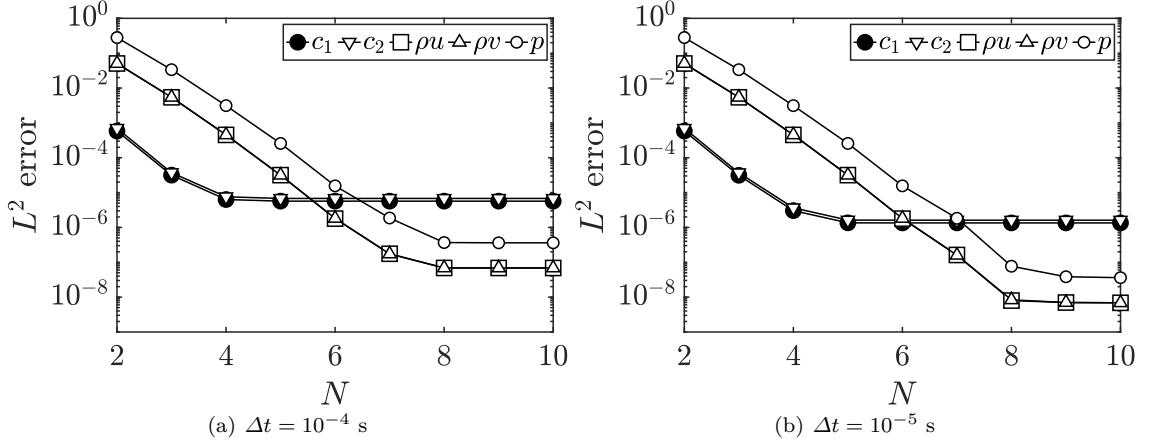


**Fig. 8** Three-phase solver: polynomial order convergence study of the manufactured solution (53). We represent the  $L^2$  errors of the two concentrations  $c_1$  and  $c_2$ ,  $x$ - and  $y$ -momentum, and pressure. The polynomial order ranges from 2 to 10, and we integrate in time until  $t_F = 0.1$  s with two time step sizes:  $\Delta t = 10^{-4}$  s and  $10^{-5}$  s. All physical parameters are given in Table 5

are written in Table 6. We observe that for the two concentrations, the convergence rates are always between  $N$  and  $N + 2$ , for  $N = 2$  and  $N = 3$ , and due to the early stagnation, as in the two-phase solver, we cannot evaluate the convergence rates for  $N = 4$  and  $N = 5$ . For the rest of the variables, as in the two-phase solver, we find that the convergence rates are always between  $N$  and  $N + 1$ , as expected.

Overall, we confirm that the scheme and its implementation are accurate for the industrial applications.

## 5.2 Two-dimensional channel

In this section, we study the three-phase flow obtained in a two-dimensional channel  $\Omega = [0, 10] \times [-0.5, 0.5]$  m. The configuration is an extension to three-phase of the two-phase channel studied in [70]. At the inlet, we introduce a heavy fluid (Phase 2, red) on the top, and a light fluid (Phase 3, black) on the bottom, both immersed in Phase 1 (white), with medium density. The vertical gravity results in the heavy fluid falling to the bottom side of the domain, while the light fluid rising to the top. The physical parameters are given in Table 7. At the inlet, we impose the inflow boundary condition, and the initial condition is  $c_1 = 1$ ,  $c_2 = c_3 = 0$ ,  $u = 1 - 4z^2$ , and  $v = w = p = 0$ . The computational domain  $\Omega$  is divided into  $15 \times 60$  elements (which is the coarsest configuration described in [70]), and we approximate the solution with  $N = 5$  polynomials. We use the split-form scheme and the IMEX time integrator with  $S_0 = 8$ , and



**Table 6** Three-phase solver: manufactured solution (53) convergence analysis: we use  $4^3$ ,  $8^3$ , and  $16^3$  meshes, and  $N = 2, 3, 4$  and 5. The final time is  $t_F = 0.1$  s, and we use the IMEX scheme with  $\Delta t = 5 \cdot 10^{-5}$  s

	Mesh	$c_1$ error	order	$c_2$ error	order	$\rho u$ error	order	$\rho v$ error	order	$p$ error	order
N=2	$4^2$	5.82E-04	–	6.97E-04	–	5.06E-02	–	5.06E-02	–	2.81E-01	–
	$6^2$	1.60E-04	3.19	1.91E-04	3.19	1.92E-02	2.39	1.92E-02	2.39	1.17E-01	2.15
	$8^2$	5.97E-05	3.42	7.15E-05	3.41	9.38E-03	2.49	9.38E-03	2.49	6.19E-02	2.22
	$12^2$	1.61E-05	3.23	1.93E-05	3.23	3.28E-03	2.59	3.28E-03	2.59	2.40E-02	2.34
	$16^2$	6.65E-06	3.07	7.97E-06	3.07	1.51E-03	2.70	1.51E-03	2.70	1.18E-02	2.47
N=3	$4^2$	3.13E-05	–	3.69E-05	–	5.41E-03	–	5.41E-03	–	3.36E-02	–
	$6^2$	3.67E-06	5.29	4.38E-06	5.26	1.30E-03	3.52	1.30E-03	3.52	9.41E-03	3.14
	$8^2$	1.49E-06	3.13	1.79E-06	3.11	4.51E-04	3.68	4.50E-04	3.68	3.65E-03	3.30
	$12^2$	1.35E-06	0.25	1.62E-06	0.25	9.55E-05	3.83	9.55E-05	3.83	9.01E-04	3.45
	$16^2$	1.35E-06	0.00	1.61E-06	0.00	3.08E-05	3.94	3.08E-05	3.94	3.20E-04	3.60
N=4	$4^2$	3.03E-06	–	3.65E-06	–	4.52E-04	–	4.52E-04	–	3.12E-03	–
	$6^2$	1.39E-06	1.93	1.66E-06	1.94	7.10E-05	4.56	7.10E-05	4.57	5.47E-04	4.30
	$8^2$	1.35E-06	0.10	1.62E-06	0.10	1.85E-05	4.67	1.85E-05	4.67	1.52E-04	4.46
	$12^2$	1.35E-06	0.00	1.61E-06	0.00	2.67E-06	4.77	2.67E-06	4.77	2.37E-05	4.58
	$16^2$	1.35E-06	0.00	1.61E-06	0.00	6.59E-07	4.87	6.59E-07	4.87	6.20E-06	4.67
N=5	$4^2$	1.35E-06	–	1.62E-06	–	3.17E-05	–	3.15E-05	–	2.57E-04	–
	$6^2$	1.35E-06	0.01	1.61E-06	0.01	3.18E-06	5.67	3.18E-06	5.66	2.83E-05	5.44
	$8^2$	1.35E-06	0.00	1.61E-06	0.00	6.23E-07	5.67	6.22E-07	5.67	5.79E-06	5.52
	$12^2$	1.35E-06	0.00	1.61E-06	0.00	6.48E-08	5.58	6.47E-08	5.58	5.81E-07	5.67
	$16^2$	1.35E-06	0.00	1.61E-06	0.00	1.50E-08	5.08	1.50E-08	5.08	1.15E-07	5.62

**Table 7** Three-phase solver: list of the parameter values used for the two-dimensional three-phase channel

$\rho_1$	$\rho_2$	$\rho_3$ (kg/m <sup>3</sup> )	$\eta_1$	$\eta_2$	$\eta_3$ (Pa·s)	$\varepsilon$ (m)
1.0	5.0	0.8	5.0E-3	1.0E-2	1.0E-2	0.0424
$M_0$ (m/s)	$c_0$ (m/s <sup>2</sup> )	$\sigma_{12}$	$\sigma_{13}$	$\sigma_{23}$ (N/m)		
1.0E-4	1.0E3	2.5E-4	2.5E-4	2.5E-4		

$$\Delta t = 3.0 \cdot 10^{-5} \text{ s.}$$

$$\begin{aligned}
c_1 &= 1 - c_2 - c_3, \\
c_2 &= \frac{1}{2} \left( 1 + \tanh \left( \frac{z - 0.3}{\varepsilon} \right) \right), \\
c_3 &= \frac{1}{2} \left( 1 - \tanh \left( \frac{z + 0.3}{\varepsilon} \right) \right), \\
u &= 1 - 4z^2, \\
v &= w = 0, \\
p &= p_{in}.
\end{aligned} \tag{54}$$

In Fig. 9 we have represented 10 snapshots of the fluid configuration, corresponding to intervals of 0.3 s. In red, we have represented the heavy fluid (Phase 2), and the light fluid (Phase 3) in black, whereas the medium density fluid (Phase 1) is white. We see that Phase 2 is prone to fall faster at the early stages because of the higher density ratio ( $\rho_2/\rho_1 = 5$ ), while the rise of Phase 3 is more subtle (although it is more pronounced in the first snapshot), since the density ratio is lower ( $\rho_3/\rho_1 = 0.8$ ).

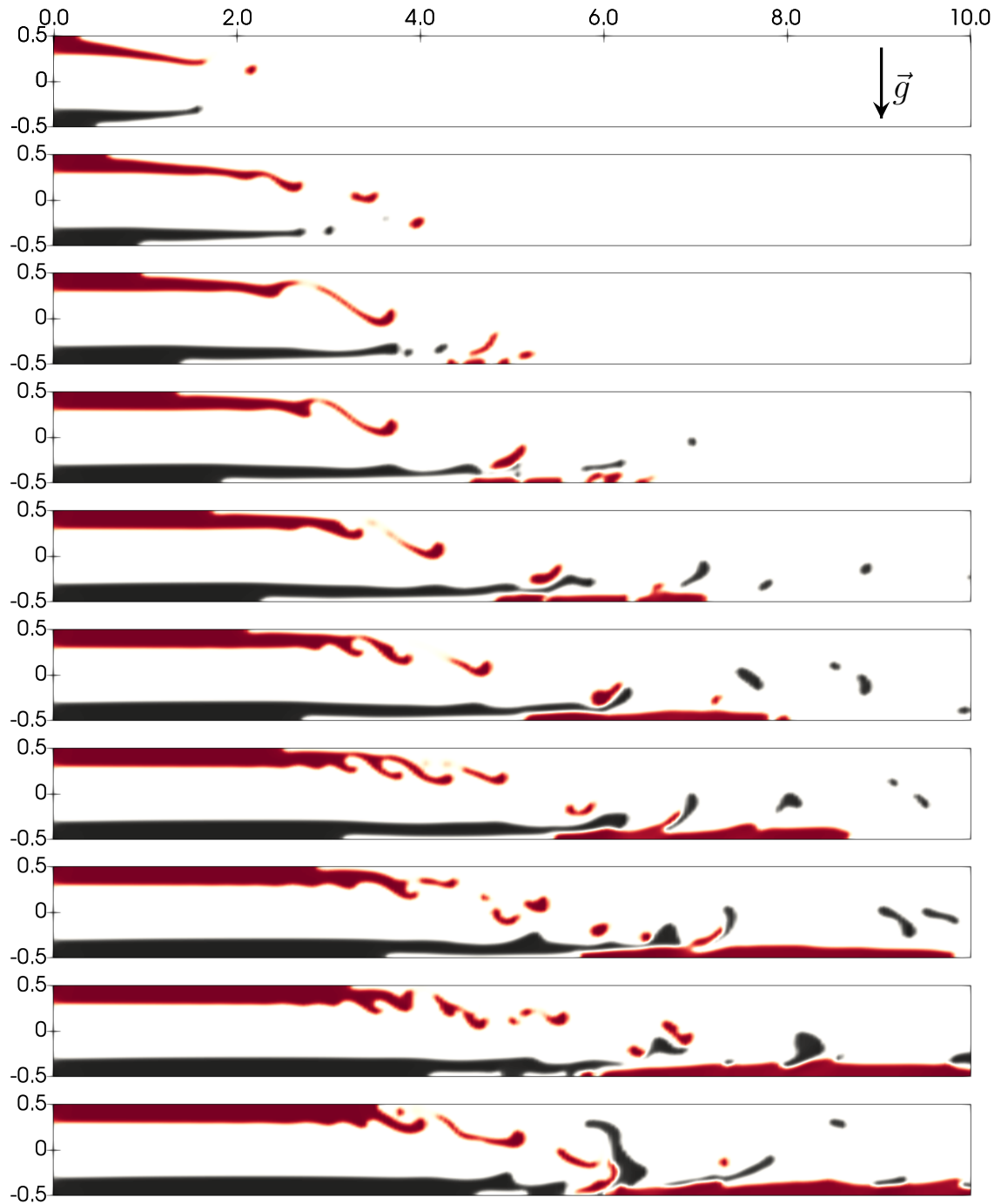


**Fig. 9** Three-phase solver: snapshots of the fluid evolution of the three-phase channel flow. We have represented the heavy fluid (Phase 2) in red, the light fluid (Phase 3) in black, and the medium density fluid (Phase 1) in white

As a result, Phase 3 forms a film in the lower part of the channel, which is then broken by droplets of Phase 2 between  $x = 4$  m and  $x = 6$  m. These droplets are a result of the Rayleigh–Taylor instability between fluids 1 and 2 in the upper part, which periodically creates droplets of Phase 2 which fall to the lower part of the channel as a result of gravitational forces. As a result, we find that the heavy fluid accumulates in the lower part of the channel, while the light fluid is scattered into bubbles which leave the domain if they are big enough, whereas the smaller ones dissolve into Phase 1.

### 5.3 Three-dimensional annular flow

In this section, we include a third phase to the annular flow simulation performed for the two-phase simplification in Sec. 4.2. Therefore, to the initial configuration with  $\rho_2 = 1$  kg/m<sup>3</sup> and  $\rho_3 = 5$  kg/m<sup>3</sup>, we add a lighter third phase with  $\rho_1 = 0.5$  kg/m<sup>3</sup>. The inflow configuration follows the description in Fig. 2. The physical parameters including superficial and slip velocities are given in Table 8. We maintain the

**Table 8** Three-phase solver: list of the parameter values used for the three-phase annular flow

$\rho_1$	$\rho_2$	$\rho_3$ (kg/m <sup>3</sup> )	$\eta_1$	$\eta_2$	$\eta_3$ (Pa·s)	$\varepsilon$ (m)
0.5	1.0	5.0	1.0E-3	5.0E-3	1.0E-2	0.0424
$M_0$ (m/s)		$c_0$ (m/s <sup>2</sup> )	$\sigma_{12}$	$\sigma_{13}$	$\sigma_{23}$ (N/m)	
9.428E-5		1.0E3	2.5E-4	2.5E-4	2.5E-4	
$V_{s,1}$	$V_{s,2}$	$V_{s,3}$	$V_{s,12}$	$V_{s,23}$ (m/s)		
1.0	3.9	0.06	0.0	10.0		

mesh used for the two-phase pipe simulations (see Sec. 4.2), and we use order  $N = 3$  polynomials. We use the IMEX time integrator with  $S_0 = 8$  and  $\Delta t = 10^{-5}$  s.

We represent the flow configuration in  $t = 3$  s in Fig. 10. The light fluid (Phase 1) on top is represented in gray, and the heavy fluid (Phase 3) is represented in blue, both immersed in Phase 2 (not represented for clarity). We see that Phase 3 describes an annular flow regime very similar to that seen in the two-phase problem. The additional phase fills the upper space, which does not fall to the lower part because of its lower density.

### 5.4 Three-dimensional T-shaped pipe intersection

Finally, we solve a T-shaped pipe junction configuration, with two inlets and one outlet. The domain features a straight upper inlet whose length is 3 m, which is then coupled to a 90° bend whose radius is 3 m. Additionally, the second inlet has a straight 5 m section, and then another 90°/3 m bend. Finally, the outlet after the T-shaped junction is a straight pipe whose length is 6 m. The diameter of the pipe is  $D = 1$  m. The computational mesh used, with 1700 elements, is represented in Fig. 11.

The physical parameters are given in Table 9. In the upper inlet, we only inject Phases 1 and 2 with superficial velocities  $V_{s,1} = V_{s,2} = 4$  m/s. In the lower inlet, we only inject Phase 3 with superficial

**Table 9** Three-phase solver: list of the parameter values used for the three-phase T-shaped pipe intersection simulation

$\rho_1$	$\rho_2$	$\rho_3$ (kg/m <sup>3</sup> )	$\eta_1$	$\eta_2$	$\eta_3$ (Pa·s)	$\varepsilon$ (m)
5.0	1.0	0.2	1.0E-5	2.5E-5	5.0E-5	0.03
$M_0$		$c_0$ (m/s <sup>2</sup> )	$\sigma_{12}$	$\sigma_{13}$	$\sigma_{23}$ (N/m)	
1.8856E-2		1.0E3	2.5E-4	2.5E-4	2.5E-4	

velocity  $V_{s,3} = 2$  m/s. Additionally, the gravity acceleration is  $\vec{g} = -1$  m/s<sup>2</sup> in x-direction. We use order  $N = 3$  polynomials and the IMEX scheme uses  $S_0 = 8$  with a time-step size  $\Delta t = 5 \cdot 10^{-5}$  s. The initial condition is a steady-state with uniform pressure  $p = 0$ , and with the pipe filled with Phase 3 ( $c_1 = c_2 = 0$ ).

We represent the evolution of the phases in Fig. 12, where we represent Phase 2 in blue, Phase 3 in gray and the space left is occupied by Phase 1. Initially the pipe is filled with Phase 3, which was chosen because it has the minimum density of the three-phase (therefore is easier for the other two phases to displace it). At the initial stages (see Fig. 12(b)), we observe the advancing front at the upper inlet. We see that Phase 2 (blue) overtakes Phase 1 at the elbow, and then both phases arrive at the main pipe at  $t \approx 1.5$  (see Fig. 12(d)). Then, Phases 1 and 2 enter the principal pipe, and they restrict the flow of Phase 3 after the T-shaped pipe intersection. The lower density Phase 3 is then confined to the wall, and phases 1 and 2 intermittently occupy the bulk of the pipe (see Fig. 12(i)).

In Fig. 13 we represent the configuration of the three-phase at the final simulation time at  $t = 7.5$  s. Both Phases 1 (Fig. 13(a)) and 2 (Fig. 13(b)) represent the bulk of the pipe, whereas Phase 3 (Fig. 13(c)) is forced to coat the pipe walls (similar to an annular flow regime). Due to the rupture of the flow of Phase 3 by the Phases 1 and 2, Phase 3 gets a counter-clockwise swirl motion around the pipe.

Finally, we represent the velocity contours at the final time  $t = 7.5$  s in Fig. 14. We can see the detachment due to the low viscosity of Phase 2 at the upper elbow, and also in the lower elbow for Phase 3. Then, after the T-shaped intersection, the flow becomes under-resolved with large velocity spots as a result of the interaction between the three phases.

Overall, we confirm the validity of the solver to compute simulations in complex three-dimensional geometries, as those found in the oil and gas industry.

## 6 Conclusions

We present a three-phase incompressible Navier-Stokes/Cahn-Hilliard system, and its discontinuous Galerkin implementation. The model uses the three-phase Cahn-Hilliard model of [1], and the incompressible Navier-Stokes with artificial compressibility of [2].

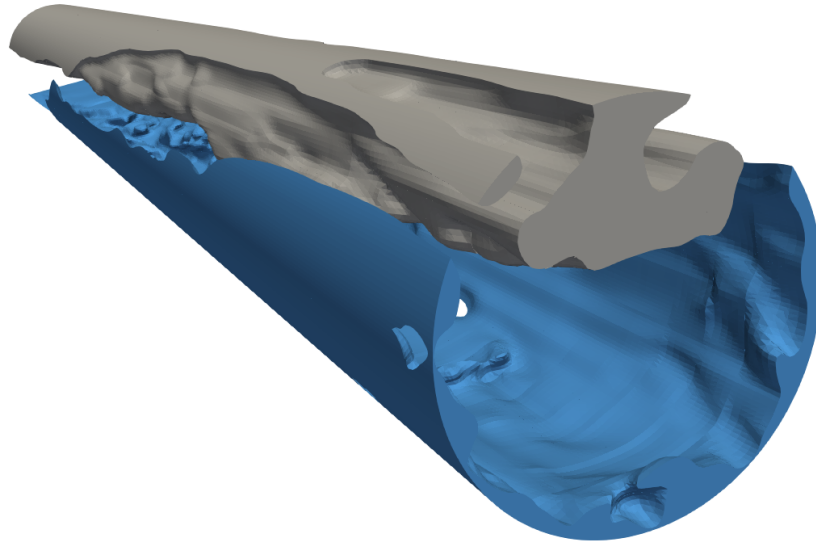
We construct a discontinuous Galerkin approximation of the equations, where we combine the scheme used for the three-phase Cahn-Hilliard model in [62] and that used for the entropy-stable incompressible Navier-Stokes equations of [2].

We validate the solver in the two-phase simplification with a manufactured solution, and solving two-phase pipe regimes. Then, it is used to solve three-phase flows: a manufactured solution, a two-dimensional channel and a three-dimensional T-shaped pipe intersection. We find that the solver has not crashed in any of the simulations once the time-step size has been appropriately chosen. We highlight the

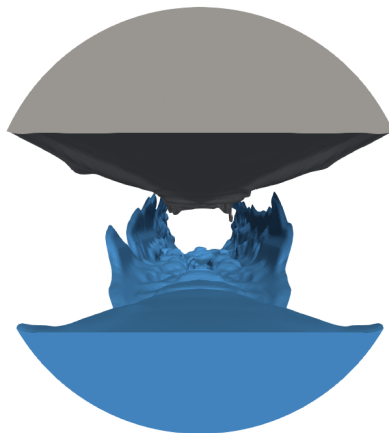
ease in the configuration of the solver and the scheme for a user, as it only requires an appropriate choice of the physical parameters and conditions, plus the choice of the polynomial order of the simulation. The rest of the numerical parameters have been proven valid in a vast range of flow conditions, and the boundary conditions are automatically set-up by the algorithm that computes the inlet profile for given superficial/slip velocities. The enhancement of the robustness added by the split-form scheme, although formally does not satisfy a discrete entropy inequality, has been addressed with numerical experiments. Although the solutions of the flows presented are under-resolved, a better resolution can be achieved by increasing the polynomial order, which avoids re-meshing the geometry.

### **Acknowledgement**

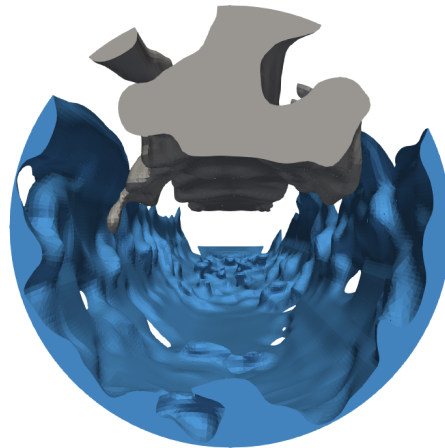
The authors acknowledge the computer resources and technical assistance provided by the Centro de Supercomputación y Visualización de Madrid (CeSViMa). The authors acknowledge Repsol Technology Lab and Universidad Politécnica de Madrid for their support and permission to publish this work. Gonzalo Rubio and Eusebio Valero acknowledge the funding received by the project SIMOPAIR (Project No. REF: RTI2018-097075-B-I00) from the Ministry of Innovation of Spain. Authors also thank Gabriel Rucabado from Repsol Technology Lab for his assistance during the execution of this work.



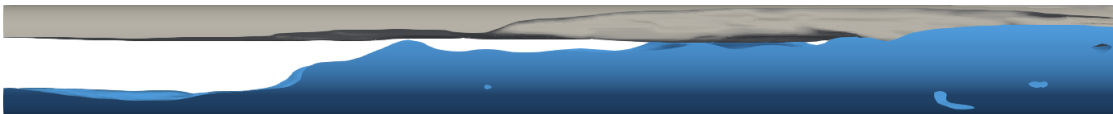
(a) Three-dimensional view



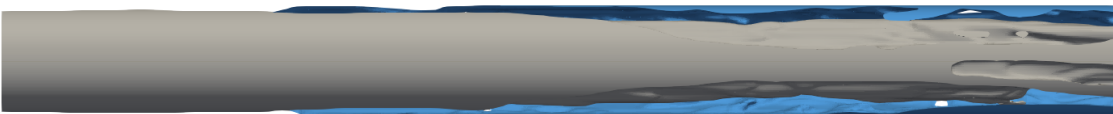
(b) Rear view



(c) Front view

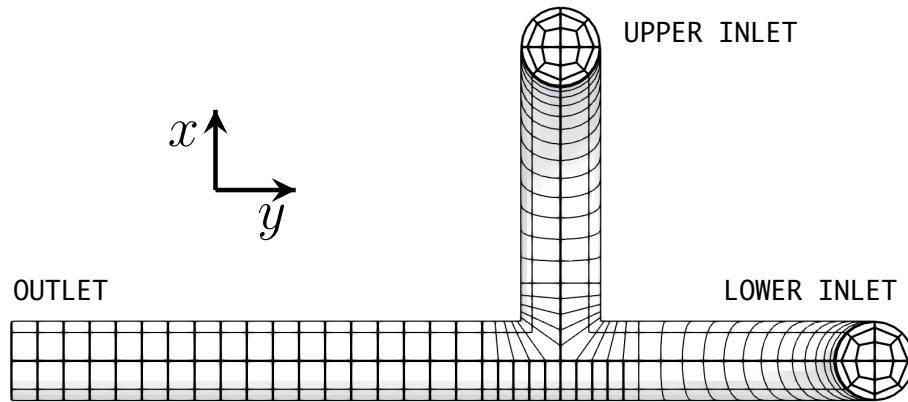


(d) Side view

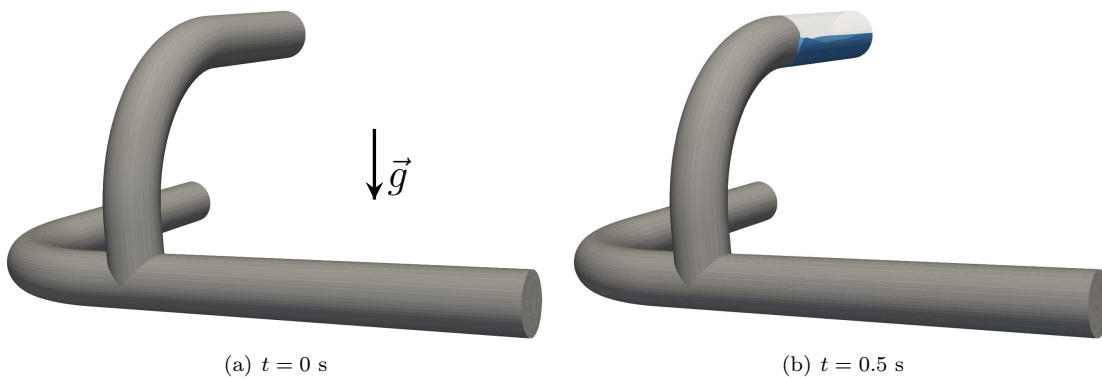


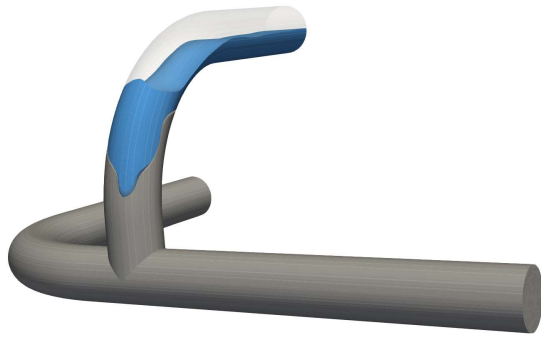
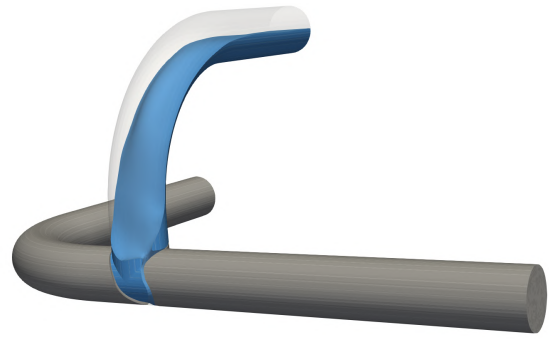
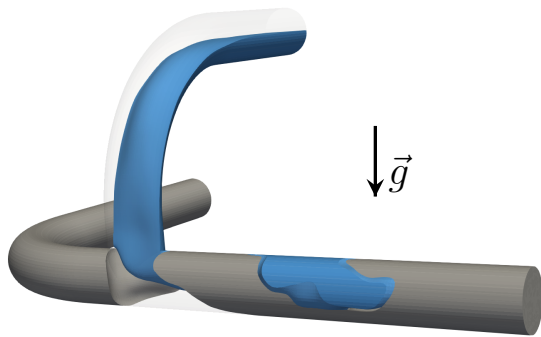
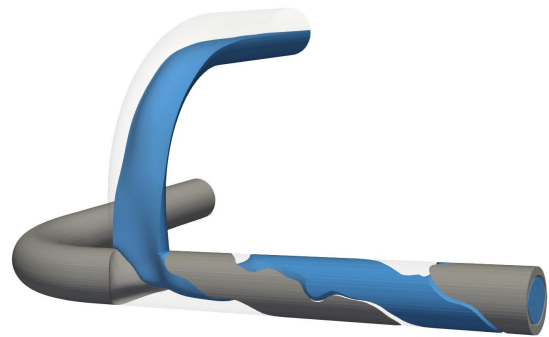
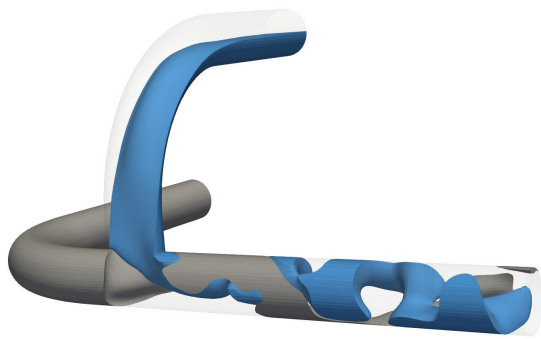
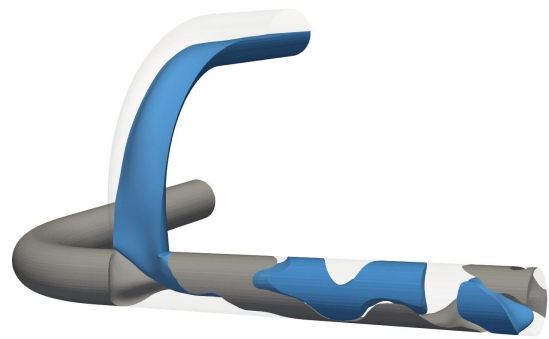
(e) Top view

**Fig. 10** Three-phase solver: three-phase annular flow simulation: the fluid configuration is represented in  $t = 3$ . The heavy fluid (Phase 3) is represented in blue, while the light fluid (Phase 1) is represented in gray



**Fig. 11** Three-phase solver: computational mesh for the T-shaped junction pipe domain, with 1700 elements



(c)  $t = 1.0$  s(d)  $t = 1.5$  s(e)  $t = 2.0$  s(f)  $t = 2.5$  s(g)  $t = 3.0$  s(h)  $t = 3.5$  s



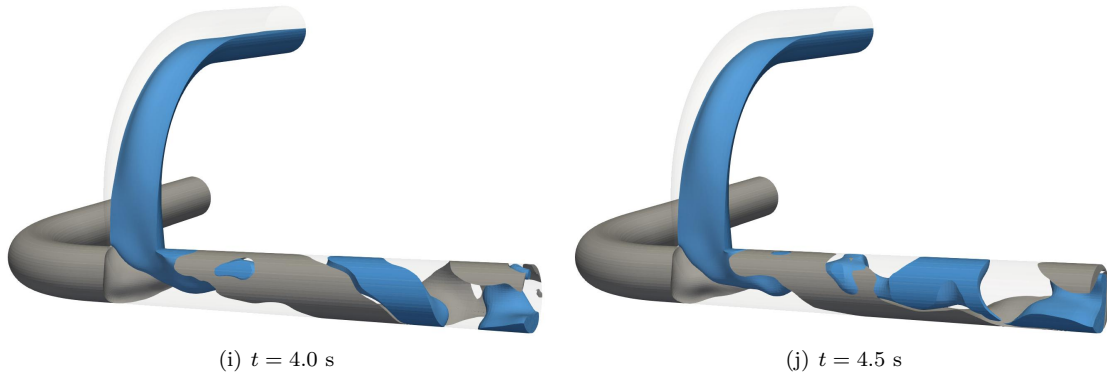
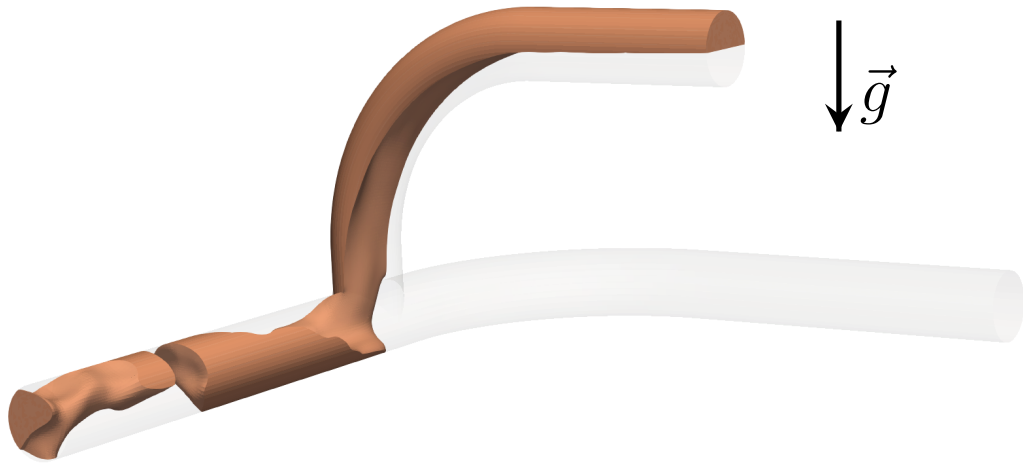


**Fig. 12** Three-phase solver: evolution of phase two (blue) and phase three (gray) for the first 4.5 seconds



(a) Phase 1



(b) Phase 2



(c) Phase 3

**Fig. 13** Three-phase solver: representation of the three-phase at the final time  $t = 7.5$

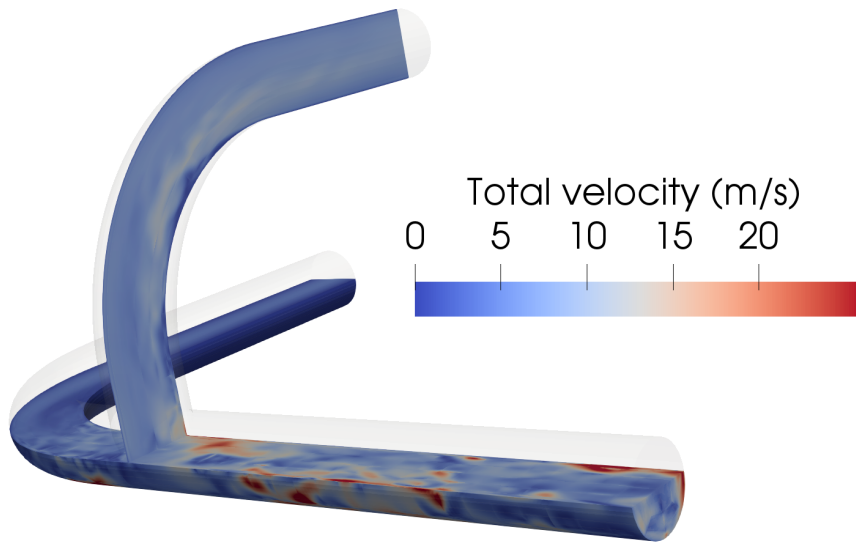


**Fig. 14** Three-phase solver: total velocity contour at the final time  $t = 7.5$  s

## References

1. F. Boyer, C. Lapuerta, Study of a three component Cahn-Hilliard flow model, *ESAIM: Mathematical Modelling and Numerical Analysis-Modélisation Mathématique et Analyse Numérique* 40 (4) (2006) 653–687.
2. J. Manzanero, G. Rubio, D. A. Kopriva, E. Ferrer, E. Valero, An entropy-stable discontinuous Galerkin approximation for the incompressible Navier-Stokes equations with variable density and artificial compressibility, *Journal of Computational Physics* 408 (2020) 109241.
3. R. Belt, E. Duret, D. Larrey, B. Djoric, S. Kalali, et al., Comparison of commercial multiphase flow simulators with experimental and field databases, in: *15th International Conference on Multiphase Production Technology*, BHR Group, 2011.
4. E. Gharaibah, A. Read, G. Scheuerer, et al., Overview of cfd multiphase flow simulation tools for subsea oil and gas system design, optimization and operation, in: *OTC Brasil, Offshore Technology Conference*, 2015.
5. C. W. Hirt, B. D. Nichols, Volume of fluid (VOF) method for the dynamics of free boundaries, *Journal of computational physics* 39 (1) (1981) 201–225.
6. M. Sussman, P. Smereka, S. Osher, A level set approach for computing solutions to incompressible two-phase flow, *Journal of Computational Physics* 114 (1) (1994) 146–159.
7. D. Jacqmin, Calculation of two-phase Navier-Stokes flows using phase-field modeling, *Journal of Computational Physics* 155 (1) (1999) 96–127.
8. D. M. Anderson, G. B. McFadden, A. A. Wheeler, Diffuse-interface methods in fluid mechanics, *Annual review of fluid mechanics* 30 (1) (1998) 139–165.
9. V. Badalassi, H. Cenicerros, S. Banerjee, Computation of multiphase systems with phase field models, *Journal of Computational Physics* 190 (2) (2003) 371–397.
10. R. Bonhomme, J. Magnaudet, F. Duval, B. Piar, Inertial dynamics of air bubbles crossing a horizontal fluid-fluid interface.
11. Y. Inoue, Y. Chen, H. Ohashi, A mesoscopic simulation model for immiscible multiphase fluids, *Journal of Computational Physics* 201 (1) (2004) 191–203.
12. B. Merriman, J. K. Bence, S. J. Osher, Motion of multiple junctions: A level set approach, *Journal of Computational Physics* 112 (2) (1994) 334–363.
13. R. I. Saye, J. A. Sethian, The Voronoi implicit interface method for computing multiphase physics, *Proceedings of the National Academy of Sciences* 108 (49) (2011) 19498–19503.
14. K. A. Smith, F. J. Solis, D. Chopp, A projection method for motion of triple junctions by level sets, *Interfaces and free boundaries* 4 (3) (2002) 263–276.
15. A. Villa, L. Formaggia, Implicit tracking for multi-fluid simulations, *Journal of Computational Physics* 229 (16) (2010) 5788–5802.
16. H.-K. Zhao, T. Chan, B. Merriman, S. Osher, A variational level set approach to multiphase motion, *Journal of Computational Physics* 127 (1) (1996) 179–195.
17. W. Zheng, J.-H. Yong, J.-C. Paul, Visual simulation of multiple unmixable fluids, *Journal of Computer Science and Technology* 22 (1) (2007) 156–160.
18. S. Zlotnik, P. Díez, Hierarchical x-fem for n-phase flow (n<sub>l</sub> 2), *Computer Methods in Applied Mechanics and Engineering* 198 (30-32) (2009) 2329–2338.
19. F. Boyer, C. Lapuerta, S. Minjeaud, B. Piar, M. Quintard, Cahn-Hilliard/Navier-Stokes model for the simulation of three-phase flows, *Transport in Porous Media* 82 (3) (2010) 463–483.

20. F. Boyer, S. Minjeaud, Numerical schemes for a three component Cahn-Hilliard model, *ESAIM: Mathematical Modelling and Numerical Analysis-Modélisation Mathématique et Analyse Numérique* 45 (4) (2011) 697–738.
21. J. Kim, Phase field computations for ternary fluid flows, *Computer methods in applied mechanics and engineering* 196 (45-48) (2007) 4779–4788.
22. J. Kim, A generalized continuous surface tension force formulation for phase-field models for multi-component immiscible fluid flows, *Computer Methods in Applied Mechanics and Engineering* 198 (37-40) (2009) 3105–3112.
23. J. Kim, Phase-field models for multi-component fluid flows, *Communications in Computational Physics* 12 (3) (2012) 613–661.
24. J. Kim, K. Kang, J. Lowengrub, et al., Conservative multigrid methods for ternary Cahn-Hilliard systems, *Communications in Mathematical Sciences* 2 (1) (2004) 53–77.
25. H. G. Lee, J.-W. Choi, J. Kim, A practically unconditionally gradient stable scheme for the n-component Cahn-Hilliard system, *Physica A: Statistical Mechanics and its Applications* 391 (4) (2012) 1009–1019.
26. S. Dong, An efficient algorithm for incompressible n-phase flows, *Journal of Computational Physics* 276 (2014) 691–728.
27. S. Dong, Wall-bounded multiphase flows of n immiscible incompressible fluids: Consistency and contact-angle boundary condition, *Journal of Computational Physics* 338 (2017) 21–67.
28. Z. Yang, S. Dong, Multiphase flows of n immiscible incompressible fluids: An outflow/open boundary condition and algorithm, *Journal of Computational Physics* 366 (2018) 33–70.
29. S. Dong, Multiphase flows of n immiscible incompressible fluids: a reduction-consistent and thermodynamically-consistent formulation and associated algorithm, *Journal of Computational Physics* 361 (2018) 1–49.
30. C. Liu, J. Shen, A phase field model for the mixture of two incompressible fluids and its approximation by a Fourier-spectral method, *Physica D: Nonlinear Phenomena* 179 (3-4) (2003) 211–228.
31. J. Lowengrub, L. Truskinovsky, Quasi-incompressible Cahn-Hilliard fluids and topological transitions, *Proceedings of the Royal Society of London. Series A: Mathematical, Physical and Engineering Sciences* 454 (1978) (1998) 2617–2654.
32. J. W. Cahn, J. E. Hilliard, Free energy of a nonuniform system. I. Interfacial free energy, *The Journal of chemical physics* 28 (2) (1958) 258–267.
33. J. Shen, On a new pseudocompressibility method for the incompressible Navier-Stokes equations, *Applied numerical mathematics* 21 (1) (1996) 71–90.
34. B. S. Hosseini, S. Turek, M. Möller, C. Palmes, Isogeometric analysis of the Navier-Stokes-Cahn-Hilliard equations with application to incompressible two-phase flows, *Journal of Computational Physics* 348 (2017) 171–194.
35. D.A. Kopriva, *Implementing spectral methods for partial differential equations*, Springer Netherlands, 2009.
36. M. F. Wheeler, An elliptic collocation-finite element method with interior penalties, *SIAM Journal on Numerical Analysis* 15 (1) (1978) 152–161.
37. E. Ferrer and R.H.J. Willden, A high order discontinuous Galerkin finite element solver for the incompressible Navier-Stokes equations, *Computers and Fluids* 46 (1) (2011) 224–230.
38. E. Ferrer and R. H.J. Willden, A high order discontinuous Galerkin - Fourier incompressible 3D Navier-Stokes solver with rotating sliding meshes, *Journal of Computational Physics* 231 (21) (2012)

- 7037–7056.
39. E. Ferrer, An interior penalty stabilised incompressible Discontinuous Galerkin - Fourier solver for implicit Large Eddy Simulations, *Journal of Computational Physics* 348 (2017) 754–775.
  40. J. Manzanero, A. M. Rueda-Ramírez, G. Rubio, E. Ferrer, The Bassi Rebay 1 scheme is a special case of the symmetric interior penalty formulation for discontinuous Galerkin discretisations with Gauss–Lobatto points, *Journal of Computational Physics* 363 (2018) 1–10.
  41. F. Fraysse, C. Redondo, G. Rubio, E. Valero, Upwind methods for the Baer–Nunziato equations and higher-order reconstruction using artificial viscosity, *Journal of Computational Physics* 326 (2016) 805–827.
  42. C. Redondo, F. Fraysse, G. Rubio, E. Valero, Artificial Viscosity Discontinuous Galerkin Spectral Element Method for the Baer–Nunziato Equations, in: *Spectral and High Order Methods for Partial Differential Equations ICOSAHOM 2016*, Springer, 2017, pp. 613–625.
  43. S. Gómez-Álvarez, A. Rivero-Jiménez, G. Rubio, J. Manzanero, C. Redondo, et al., Novel Coupled Cahn–Hilliard Navier–Stokes Solver for the Evaluation of Oil and Gas Multiphase Flow, in: *BHR 19th International Conference on Multiphase Production Technology*, BHR Group, 2019.
  44. J. Manzanero, G. Rubio, D. A. Kopriva, E. Ferrer, E. Valero, Entropy-stable discontinuous Galerkin approximation with summation-by-parts property for the incompressible Navier–Stokes/Cahn–Hilliard system, *Journal of Computational Physics* (2020) 109363.
  45. J. Manzanero, C. Redondo, G. Rubio, E. Ferrer, E. Valero, S. Gómez-Álvarez, Á. Rivero-Jiménez, A high-order discontinuous Galerkin solver for multiphase flows, in: *Spectral and High Order Methods for Partial Differential Equations ICOSAHOM 2018*, Springer, Cham, 2020, pp. 313–323.
  46. J. S. Hesthaven, T. Warburton, *Nodal discontinuous Galerkin methods: algorithms, analysis, and applications*, Springer Science and Business Media, 2007.
  47. G. Gassner, D. A. Kopriva, A comparison of the dispersion and dissipation errors of Gauss and Gauss–Lobatto discontinuous Galerkin spectral element methods, *SIAM Journal on Scientific Computing* 33 (5) (2011) 2560–2579.
  48. R. C. Moura, S. J. Sherwin, J. Peiró, Linear dispersion–diffusion analysis and its application to under-resolved turbulence simulations using discontinuous Galerkin spectral/hp methods, *Journal of Computational Physics* 298 (2015) 695–710.
  49. J. Manzanero, G. Rubio, E. Ferrer, E. Valero, Dispersion–dissipation analysis for advection problems with nonconstant coefficients: Applications to discontinuous Galerkin formulations, *SIAM Journal on Scientific Computing* 40 (2) (2018) A747–A768.
  50. J. Manzanero, E. Ferrer, G. Rubio, E. Valero, Design of a Smagorinsky spectral vanishing viscosity turbulence model for discontinuous Galerkin methods, *Computers and Fluids* (2020) 104440.
  51. D. A. Kopriva, Metric identities and the discontinuous spectral element method on curvilinear meshes, *Journal of Scientific Computing* 26 (3) (2006) 301.
  52. M. Kompenhans, G. Rubio, E. Ferrer, and E. Valero, Comparisons of p–adaptation strategies based on truncation– and discretisation–errors for high order discontinuous Galerkin methods, *Computers and Fluids* 139 (2016) 36 – 46, 13th USNCCM, International Symposium of High-Order Methods for Computational Fluid Dynamics - A special issue dedicated to the 60th birthday of Professor David Kopriva.
  53. M. Kompenhans, G. Rubio, E. Ferrer, and E. Valero, Adaptation strategies for high order discontinuous Galerkin methods based on tau-estimation, *Journal of Computational Physics* 306 (2016) 216 – 236.

54. A. M. Rueda-Ramírez, J. Manzanero, E. Ferrer, G. Rubio, E. Valero, A p-multigrid strategy with anisotropic p-adaptation based on truncation errors for high-order discontinuous Galerkin methods, *Journal of Computational Physics* 378 (2019) 209–233.
55. G.J. Gassner, A.R. Winters and D.A. Kopriva, Split form nodal discontinuous Galerkin schemes with Summation-By-Parts property for the compressible Euler equations, *Journal of Computational Physics*, in Press.
56. A.R. Winters and G.J. Gassner, Affordable, entropy conserving and entropy stable flux functions for the ideal MHD equations, *Journal of Computational Physics* 304 (2016) 72 – 108.
57. J. Manzanero, G. Rubio, E. Ferrer, E. Valero, D. A. Kopriva, Insights on aliasing driven instabilities for advection equations with application to Gauss–Lobatto discontinuous Galerkin methods, *Journal of Scientific Computing* 75 (3) (2018) 1262–1281.
58. G. J. Gassner, A. R. Winters, F. J. Hindenlang, D. A. Kopriva, The BR1 scheme is stable for the compressible Navier–Stokes equations, *Journal of Scientific Computing* 77 (1) (2018) 154–200.
59. J. Manzanero, G. Rubio, D. A. Kopriva, E. Ferrer, E. Valero, A free-energy stable nodal discontinuous Galerkin approximation with summation-by-parts property for the Cahn–Hilliard equation, *Journal of Computational Physics* 403 (2020) 109072.
60. Y. Xia, Y. Xu, C.-W. Shu, Local discontinuous Galerkin methods for the Cahn–Hilliard type equations, *Journal of Computational Physics* 227 (1) (2007) 472–491.
61. S. Dong, An efficient algorithm for incompressible N-phase flows, *Journal of Computational Physics* 276 (2014) 691–728.
62. J. Manzanero, C. Redondo, G. Rubio, E. Ferrer, A. Jiménez, A discontinuous Galerkin approximation for a wall-bounded consistent three-component Cahn–Hilliard flow model, Under review in *Computers and Fluids*.
63. F. Boyer, C. Lapuerta, Study of a three component Cahn–Hilliard flow model, *ESAIM: Mathematical Modelling and Numerical Analysis* 40 (4) (2006) 653–687.
64. J. Shen, Pseudo-compressibility methods for the unsteady incompressible navier-stokes equations, in: *Proceedings of the 1994 Beijing symposium on nonlinear evolution equations and infinite dynamical systems*, 1997, pp. 68–78.
65. J. Shen, X. Yang, Energy stable schemes for Cahn–Hilliard phase-field model of two-phase incompressible flows, *Chinese Annals of Mathematics, Series B* 31 (5) (2010) 743–758.
66. G.J. Gassner, A skew-symmetric discontinuous Galerkin spectral element discretization and its relation to SBP-SAT finite difference methods, *SIAM Journal on Scientific Computing* 35 (3) (2013) 1233–1256.
67. F. Bassi, F. Massa, L. Botti, A. Colombo, Artificial compressibility Godunov fluxes for variable density incompressible flows, *Computers and Fluids* 169.
68. K. Shahbazi, Short note: An explicit expression for the penalty parameter of the interior penalty method, *Journal of Computational Physics* 205 (2) (2005) 401–407.
69. Y. Shi, X.-P. Wang, Modeling and simulation of dynamics of three-component flows on solid surface, *Japan Journal of Industrial and Applied Mathematics* 31 (3) (2014) 611–631.
70. F. Xie, X. Zheng, M. S. Triantafyllou, Y. Constantinides, Y. Zheng, G. E. Karniadakis, Direct numerical simulations of two-phase flow in an inclined pipe, *Journal of Fluid Mechanics* 825 (2017) 189–207.
71. Y. Taitel, A. Dukler, A model for predicting flow regime transitions in horizontal and near horizontal gas-liquid flow, *AICHE journal* 22 (1) (1976) 47–55.

- 
72. T.C. Fisher and M.H. Carpenter, High-order entropy stable finite difference schemes for nonlinear conservation laws: Finite domains, *Journal of Computational Physics* 252 (2013) 518–557.